Modelling the inner disc of the Milky Way with manifolds - I. A first step

Romero-Gomez, M.; Athanassoula, E.; Antoja Castelltort, Teresa; Figueras, F.

Published in:
Monthly Notices of the Royal Astronomical Society

DOI:
10.1111/j.1365-2966.2011.19569.x

Publication date:
2011

Monthly Notices
of the
ROYAL ASTRONOMICAL SOCIETY

Mon. Not. R. Astron. Soc. **418,** 1176–1193 (2011) doi:10.1111/j.1365-2966.2011.19569.x

Modelling the inner disc of the Milky Way with manifolds – I. A first step

M. Romero-Gómez,[1⋆] E. Athanassoula,[2] T. Antoja[3] and F. Figueras[1]

[1]*Dept. d'Astronomia i Meteorologia, Institut de Ciències del Cosmos (ICC), Universitat de Barcelona (IEEC-UB), Martí i Franquès 1, E08028 Barcelona, Spain*
[2]*Laboratoire d'Astrophysique de Marseille (LAM), UMR6110, CNRS/Université de Provence, Technopôle de Marseille Etoile, 38 rue Frédéric Joliot Curie, 13388 Marseille Cédex 20, France*
[3]*Kapteyn Astronomical Institute, University of Groningen, PO Box 800, 9700 AV Groningen, the Netherlands*

Accepted 2011 August 2. Received 2011 August 2; in original form 2011 April 11

ABSTRACT

We study the bar-driven dynamics in the inner part of the Milky Way by using invariant manifolds. This theory has been successfully applied to describe the morphology and kinematics of rings and spirals in external galaxies, and now, for the first time, we apply it to the Milky Way. In particular, we compute the orbits confined by the invariant manifolds of the unstable periodic orbits located at the ends of the bar. We start by discussing whether the *COBE*/Diffuse Infrared Background Experiment (DIRBE) bar and the Long bar compose a single bar or two independent bars and perform a number of comparisons which, taken together, argue strongly in favour of the former. More specifically, we favour the possibility that the so-called *COBE*/DIRBE bar is the boxy/peanut bulge of a bar whose outer thin parts are the so-called Long bar. This possibility is in good agreement both with observations of external galaxies, with orbital structure theory and with simulations. We then analyse in detail the morphology and kinematics given by five representative Galactic potentials. Two of these have a Ferrers bar, two have a quadrupole bar and the last one a composite bar. We first consider only the *COBE*/DIRBE bar and then extend it to include the effect of the Long bar. We find that the large-scale structure given by the manifolds describes an inner ring, whose size is similar to the near and far 3-kpc arm, and an outer ring, whose properties resemble those of the Galactic Molecular Ring. We also analyse the kinematics of these two structures, under the different Galactic potentials, and find they reproduce the relevant overdensities found in the galactic longitude–velocity CO diagram. Finally, we consider for what model parameters, the global morphology of the manifolds may reproduce the two outer spiral arms. We conclude that this would necessitate either more massive and more rapidly rotating bars, or including in the potential an extra component describing the spiral arms.

Key words: Galaxy: bulge – Galaxy: disc – Galaxy: evolution – Galaxy: kinematics and dynamics – Galaxy: structure – galaxies: spiral.

1 INTRODUCTION

The large-scale structure of the Milky Way (MW) disc has been under study for many years. The *COBE*/Diffuse Infrared Background Experiment (DIRBE; Weiland et al. 1994) and *Spitzer*/Galactic Legacy Infrared Mid-Plane Survey Extraordinaire (GLIMPSE; Churchwell et al. 2009) missions provided infrared information on the global structure of the inner Galaxy. Even though these studies have provided some light, the large-scale structure of the MW disc proves to be highly complex. Near- and mid-infrared (IR) low-resolution images detected the *COBE*/DIRBE bar (Weiland et al. 1994), also referred to as the triaxial bulge or the *COBE*/DIRBE bar. Near-IR red clump giants of the mid-plane revealed the existence of a second bar (Hammersley et al. 2000; López-Corredoira et al. 2007; Cabrera-Lavers et al. 2008), and confirmed by GLIMPSE (Benjamin et al. 2005), usually referred to as the Long bar. Observations suggest two other large-scale structures towards the inner parts of the Milky Way, namely the near and far 3-kpc arms (Kerr 1964; Dame & Thaddeus 2008) and the Galactic Molecular Ring (GMR; Clemens, Sanders & Scoville 1988). Although their characteristics or even their existence are currently being under debate (Dame & Thaddeus 2011), here we aim to bring some light given the observed characteristics up-to-date. The near and far 3-kpc arms were detected using the H I 21-cm line and CO emission surveys and extend roughly parallel to the *COBE*/DIRBE bar, whereas the position of the GMR is not so well determined. Clemens et al. (1988) suggested it is located at ∼5.5 kpc from the Galactic Centre, while

⋆E-mail: mromero@am.ub.es

other authors suggest it is located about halfway to the Galactic Centre (Binney & Merrifield 1998; Dame, Hartmann & Thaddeus 2001; Rathborne et al. 2009).

There has been a lot of effort to determine the bar and spiral arm characteristics, both from the observational and theoretical point of view. Debattista, Gerhard & Sevenster (2002) and Sevenster (2002) use a sample of ∼250 bright OH/IR stars of the inner Galaxy to determine the pattern speed of the *COBE*/DIRBE bar, while the CO emission and the 21-cm line of neutral hydrogen map the galactic longitude–velocity (l, v) diagram (Dame et al. 2001; Dame & Thaddeus 2008; Vallée 2008). The spiral arms and rings of the Galaxy appear as overdensities in such diagrams. From the theoretical point of view, several works use hydrodynamics simulations to constrain the Galaxy parameters and to reproduce the observed (l, v) diagram (e.g. Englmaier & Gerhard 1999; Rodríguez-Fernández & Combes 2008; Baba, Saitoh & Wada 2010). From the orbits point of view, Habing et al. (2006) compute a library of orbits, some of which reproduce the overdensities in the inner longitudes of the (l,v) diagram, while Green et al. (2011) study in detail the shape of the 3-kpc arm concluding that it can be approximated by an elliptical ring. Test particle simulations have recently been used to study the velocity distribution function in the solar neighbourhood and to use it to constrain the characteristics of the bar and/or spiral arms (Dehnen 2000a, hereafter Dehnen00; Fux 2001, hereafter Fux01; Chakrabarty 2007; Antoja et al. 2009; Minchev et al. 2010).

In this paper we will use an approach which is novel for our Galaxy, namely that of invariant manifolds. In a previous set of papers we developed the method and techniques that we will use here and also applied them to the study of spirals and rings in external galaxies (see Romero-Gómez et al. 2006, 2007; Athanassoula, Romero-Gómez & Masdemont 2009a; Athanassoula et al. 2009b, 2010, hereafter Papers I–V, respectively). The invariant manifolds are linked to the presence of the Lagrangian points L_1 and L_2 of a barred system and they can reproduce the observed structures of rings and spiral arms. In Papers I–V, we studied in detail the characteristics of the orbits confined by such invariant manifolds and we analysed both their morphology and kinematics so as to compare them to the rings and spiral arms in external barred galaxies. Invariant manifolds, albeit in a quite different way than what we have here and Papers I–V, have also been used by Tsoutsis et al. (2009) to model three barred galaxies, NGC 3992, NGC 1073 and NGC 1398 and by Patsis, Kalapotharakos & Grosbol (2010) to perform an orbital analysis of NGC 1300.

Here we use the invariant manifolds to compute a family of orbits of a wide range of energies and to study their morphology and their kinematics. We want to evaluate whether the invariant manifolds can provide an alternative, plausible model for the inner part of the MW disc. By using MW analytical potentials recently used in the literature, we try to answer the following questions. Can observations be plausibly interpreted by manifolds? Can the latter provide an alternative interpretation of the inner structure of the MW? Which are the requirements the potential has to fulfil in order to reproduce the rings and spiral arms of the MW? In a future paper we will examine whether the combination of the manifolds and observations can constrain the MW bar properties.

In order to compute the orbits confined by the manifolds we must first fix the Galactic potential. We have chosen the most representative analytical potentials used to describe a *COBE*/DIRBE bar, namely a Ferrers bar (Ferrers 1877), a quadrupole bar (Binney & Tremaine 2008) and a composite bar (Pichardo, Martos & Moreno 2004, hereafter PMM04). Deliberately, we consider studies where the authors have tuned one of these three types of potentials to the *COBE*/DIRBE bar, and we use the same set of parameters as they do.

The paper is organized as follows. In Section 2, we discuss whether our Galaxy has a single or a double bar, using arguments from the morphology of external galaxies, from orbital structure theory and from N-body simulations. We also describe the models and compare them in detail in terms of forces. In Section 3, we give a brief summary of the dynamics driven by the unstable Lagrangian points and, in particular, the definition of the invariant manifolds. We also give a brief summary of the main relevant results found in Papers I–V. In Section 4, we compute the invariant manifolds for the selected models and we analyse them in terms of morphology and kinematics. The results are compared to the observables in Section 4.3. In Section 5, we explore the parameter space and determine in which cases the manifolds could reproduce outer spiral arms. Finally, we give a short summary and conclusions in Section 6. In the appendix, we describe in detail the analytical models and give the default parameters used.

2 MODELLING THE GALACTIC POTENTIAL

2.1 Analytical models

There are several analytical models in the literature used to model the MW Galaxy. They essentially consist of an axisymmetric plus a one-bar component. Each model has been constructed to model the MW and in the appendix of this paper we give a brief description of the potentials used and their default parameters. We want to stress here that we will consider the same parameters as these studies. The axisymmetric component describes the disc, halo and bulge of the Galaxy and in each model it is modelled in a different way.

The models considered in this paper are the following.

(i) Melnik & Rautiainen (2009, hereafter MR09) and Gardner & Flynn (2010, hereafter GF10) both use a Ferrers bar (Ferrers 1877), though the purpose of each of the papers is very different. The former uses the bar potential in test particle simulations to model the kinematics of the outer rings and spirals of the Galaxy and to compare it with the residual velocities of OB associations in the Perseus and Sagittarius regions. The latter studies the effect of the bar parameters on the kinematic substructures found in the velocity plane of the solar neighbourhood.

(ii) Dehnen00 and Fux01 both use a quadrupole bar, but with different model parameters, to study the effect of the *COBE*/DIRBE bar on the local disc stellar kinematics. Such potentials are also often referred to as ad hoc potentials, since they are not obtained from any density distribution.

(iii) The composite bar of PMM04 consists of a set of prolate ellipsoids, superposed so that the surface density matches the mass distribution obtained by the *COBE*/DIRBE mission, and from which the potential and forces are derived. The authors compute in detail the families of orbits given by this potential and use surfaces of section to characterize the bar structure.

In order to fix the parameters of each model, the authors take into account the available relevant observational data. Even though there is a lot of uncertainty in these data, a range of possible values can be determined. The semimajor axis of the *COBE*/DIRBE bar or Galactic bulge is ∼3.1–3.5 kpc and its aspect ratio of 10:4:3 (length:width:height), as estimated by *COBE*/DIRBE (Weiland et al. 1994; Freudenreich 1998; Gerhard 2002). Several studies fix the mass of the *COBE*/DIRBE bar in the range $1–2 \times 10^{10}\,M_{\odot}$ (Matsumoto et al. 1982; Kent 1992; Dwek et al. 1995; Zhao 1996;

Weiner & Sellwood 1999). The relative orientation of the bar with respect to the Galactic Centre–Sun is not well established, although most observations [Two Micron All Sky Survey (2MASS) star counts or red clump giants] and models (based on *COBE*/DIRBE and *Spitzer*/GLIMPSE) agree it lies roughly within the range of 15°–30° (e.g. Dwek et al. 1995; Binney, Gerhard & Spergel 1997; Stanek et al. 1997; Englmaier & Gerhard 1999; Fux 1999; Bissantz & Gerhard 2002; Bissantz, Englmaier & Gerhard 2003; Babusiaux & Gilmore 2005; Benjamin et al. 2005; López-Corredoira, Cabrera-Lavers & Gerhard 2005; Churchwell et al. 2009). Here we choose 20° as a representative value. The pattern speed obtained by the studies mentioned in the Introduction lies within the range $\Omega_b = 35$–$60\,\mathrm{km\,s^{-1}\,kpc^{-1}}$ although higher values are favoured (see Gerhard 2011 for a review). As for the Long bar, it is somewhat longer than the *COBE*/DIRBE bar with a semimajor axis of ∼4–4.5 kpc and an aspect ratio of 10:1.54:0.26 (Hammersley et al. 2000). The mass of the Long bar is less than the mass of the *COBE*/DIRBE bar. It is estimated to be around $6 \times 10^9\,M_\odot$, i.e. about 2/3 that of the *COBE*/DIRBE bar (Hammersley et al. 2000; GF10). The relative orientation from the Galactic Centre–Sun line is estimated observationally to be ∼40° (Hammersley et al. 2000; Benjamin et al. 2005; López-Corredoira et al. 2007; Cabrera-Lavers et al. 2008). Note that the observational sources used to constrain the parameters of the *COBE*/DIRBE and the Long bar are different. These could, in principle, lead to somewhat different definitions of bar length. However, according to Freudenreich (1998) for the *COBE*/DIRBE bar and Hammersley et al. (2000) for the Long bar, both give estimates of the bar half-length. Even though these estimates are subject to observational errors, the ratio of the two values will not change significantly.

2.2 How many bars does our Galaxy have?

A considerable fraction of external barred galaxies are known to have two bars: a primary or main bar and a secondary or inner bar. This fraction depends on the galaxy's Hubble type, the quality of the sample images, and other factors, but fractions of the order of a third or a fourth are quite reasonable. Could it be that our Galaxy is one of these? In order to pursue this line further, one needs to make sure that the properties of the *COBE*/DIRBE bar and the Long bar are compatible with those of galaxies with double bars. Can we safely assume that the Long bar is the main bar and that the *COBE*/DIRBE bar is the secondary bar?

Several properties of inner bars have been well studied (e.g. Erwin & Sparke 2002; Laine et al. 2002; Erwin 2011) and some major trends have been found. The strongest constraints come from the bar length. Inner bars are quite small, with a semimajor axis between 100 pc and 1.2 kpc, with median size around 500 pc. Typically their relative length is about 12 per cent of that of the main bar. The sample of Erwin (2011) contains 64 galaxies with double bars and out of these only two have a secondary bar longer than 22 per cent of the primary, and none longer than 30 per cent. This contrasts strongly with the numbers for our Galaxy, where the length of the bar semimajor axis is 3.1–3.5 and ∼4 kpc for the *COBE*/DIRBE and for the Long bar, respectively. Thus the length of the *COBE*/DIRBE bar is more than 10σ beyond the values found for the inner bars of external galaxies. Furthermore, the relative length of the *COBE*/DIRBE bar relative to the Long bar is ∼0.8, again more than 10σ out of the distribution found from external galaxies. Double bars have also been found in simulations (Heller, Shlosman & Athanassoula 2007; Shen & Debattista 2009) and their parameters are in good agreement with those of observed double bars and in disagreement with the values for our Galaxy.

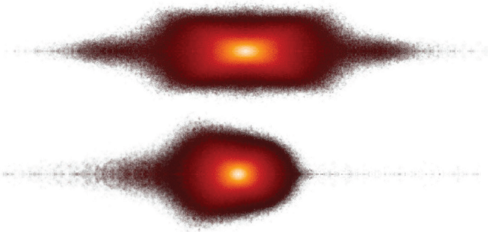

Figure 1. Two edge-on views of a bar from a simulation (see text). The upper panel shows a side-on view, and the bottom one a view from an angle near the bar major axis. In both cases the views are perspective and thus the relative thickness of the inner and outer parts should be inferred only from the upper panel.

So one can reasonably exclude that the Long and the *COBE*/DIRBE bar form a double bar system, because their properties are very far from those of double bars in external galaxies and simulations, making the two incompatible.[1] So then what is it? The data give us an important clue for that. Namely the ratio of the major- to z-semi-axis of the bar is ∼0.3 for the *COBE*/DIRBE bar and ∼0.03 for the Long bar, i.e. *the Long bar is very thin* and *the COBE/DIRBE bar is very thick*. Let us therefore examine the alternative that there is only one bar in the Galaxy and that the *COBE*/DIRBE bar is simply the part which corresponds to the boxy/peanut bulge and the Long bar the outer part of this bar. This geometry has been already discussed for external galaxies in e.g. Athanassoula (2005) and Athanassoula & Beaton (2006) and was first proposed for our Galaxy by Athanassoula (2006, 2008). Cabrera-Lavers et al. (2007) tested this suggestion using their red clump giants measurements. We will discuss here further what the relevant orbital structure studies and N-body simulations imply.

Pfenniger (1984) and Skokos, Patsis & Athanassoula (2002a,b) studied the building blocks of bars, i.e. the periodic orbits, in 3D. They found that the third dimension introduced considerable complexity to the orbital structure. Whereas in 2D it is the orbits of the x_1 family that are the backbone of the bar (Contopoulos & Papayannopoulos 1980; Athanassoula et al. 1983), in 3D we have a tree of 2D and 3D families bifurcating from the x_1 (Skokos et al. 2002a,b). Each of these families has its own horizontal and vertical extent. Since the extent of the box/peanut will in general be determined by a *different family* than that determining the length of the bar, it is natural for their lengths to be different. Furthermore, the ratio of the lengths predicted in this way (Patsis, Skokos & Athanassoula 2002) is in good agreement with that measured for the *COBE*/DIRBE bar and the Long bar (0.8).

This structure has also been seen in a number of simulations, where the bar forms very thin and after a while a vertical instability develops and creates the boxy/peanut feature (e.g. Binney 1981; Combes et al. 1990; Athanassoula 2005; Martinez-Valpuesta, Shlosman & Heller 2006). Results from one such simulation are shown in Fig. 1 (see the appendix for the details of the simulation). This is given as an illustration and not as a model of our Galaxy.

[1] Alard (2001), however, found evidence for a small lopsided bar in our Galaxy, whose size is well compatible with those of inner bars. This would then be the secondary bar of the Galactic double bar system, while the primary would be constituted of the *COBE*/DIRBE bar and the Long bar together.

In the upper panel we give the side-on view[2] of the bar component. For clarity, the remaining disc, as well as the halo, is not displayed. This shows clearly that the thick part of the bar (i.e. the boxy/peanut bulge) is less extended than the thin part and that the thin part protrudes on either side of it. It also gives an estimate of the relative vertical thickness of the inner and outer parts, although this could vary from one model to another. Note that the thin and thick part are *parts of the same bar*, and do not constitute two separate components. Furthermore, both orbital theory and simulations show that, in the present scenario of box/peanut formation, there *must* be a thin part of the bar extending further than the box/peanut.

In the lower panel of Fig. 1 the bar is viewed from an angle much nearer to end-on.[3] We do not claim that either the model, or the angle of the line of sight with respect to the bar major axis is necessarily the correct one. This projection, nevertheless, illustrates roughly how one could be mistaken into considering the poxy/peanut feature and the thin outer part of this bar as two separate components.[4]

By visualizing a simulation from many viewing angles, it is possible to realize the geometry of the object, but this is not possible for real galaxies, where only one viewing angle is possible for each case. Thus, in near face-on galaxies we can clearly see the bar, while in near side-on ones we can see the boxy/peanut bulge. There are, however, viewing angles which are near edge-on, but not quite, and where both the boxy/peanut shape and the outer thin bar are visible. The most interesting inclination range is between 60° and 80°. Several examples have already been discussed in the literature, such as NGC 7582 with an inclination angle of about 65° (Quillen et al. 1997), NGC 4442 (Bettoni & Galletta 1994) at approximately 72° and M31 at about 77° (Athanassoula & Beaton 2006). In these cases it is possible to get information on the ratio of lengths of the box/peanut and bar. For M31, where this was specifically measured with the help of cuts (Athanassoula & Beaton 2006), it was found to be ∼0.7, in good agreement with the value found for our Galaxy. Lütticke, Dettmar & Pohlen (2000) made a detailed morphological and photometrical study of a sample of 60 edge-on galaxies, also using cuts, and found that the ratio of boxy/peanut length to bar length depends on the specific morphology of boxy/peanut bulge and, therefore, on bar strength. For peanuts, this ratio is 0.53 ± 0.08, for clear boxes 0.63 ± 0.08 and for box-like shapes 0.71 ± 0.1. According to these numbers our Galaxy would be more box like, but it should be kept in mind that these statistics are based on very few objects (21 in total, for this measurement) and the scatter quite high.

The above arguments seem to exclude the possibility that the Long bar and the *COBE*/DIRBE bar are the primary and secondary bars of a double bar system, since the bar lengths and length ratios disagree strongly both with observations of external galaxies and with simulations. Double systems with bars of comparable length have never been observed either in any external galaxy or in any simulation. It would thus be very hazardous to assume that our Galaxy is the only one known to have such a feature. On the other hand, the alternative that the *COBE*/DIRBE and the Long bar are parts of a single bar is in good agreement with observations, with orbital structure and with simulations. It is thus reasonable to favour this second alternative.

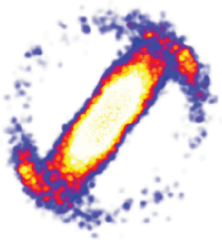

Figure 2. Face-on view of a simulation. This is not a model built specifically to represent our Galaxy, but is a clear example of a snapshot with a short leading ring segment emanating from the end of the bar (see text). In this figure the rotation is clockwise to facilitate comparison with our Galaxy.

Yet one inconsistency could still remain, concerning the position angles of the bar(s). The angle between the major axis of the *COBE*/DIRBE bar and the Galactic Centre–Sun line has been estimated to be roughly in the range ∼15° to ∼30°. First observations of the corresponding angle for the Long bar give an estimate of ∼40° (Hammersley et al. 2000; Benjamin et al. 2005; López-Corredoira et al. 2007; Cabrera-Lavers et al. 2008), while more recent work favours angles around 25° to 35° (Zasowski, Benjamin & Majewski, private communication). The uncertainties are such that the observations could be in agreement with the solution checked here, particularly since structures such as spiral arm or ring segments could contribute to the observed Long bar signal. In particular, we stress that in many *N*-body simulations there is often, within the inner ring a short, leading segment (see e.g. Athanassoula & Misiriotis 2002, and Fig. 2). Furthermore, in many *N*-body simulations and galaxies seen near face-on the boxy/peanut bulge is fatter (i.e. more extended perpendicular to the bar major axis) than the thin outer part of the bar. A more accurate answer would necessitate a detailed comparison of a large number of simulations to the observations. It would be useful to do this work using the Marseille library of high-resolution barred galaxy simulations run by one of us (EA).

2.3 Intercomparing the various models

For each model we consider three cases. In the first case, the non-axisymmetric component describes only the *COBE*/DIRBE bar or boxy/peanut bulge located at an angular separation of 20° with respect to the Galactic Centre–Sun line. We will refer to this set of models as case 1. From the discussion in the previous section we expect this to have a weaker bar than it should, since the outer parts, i.e. the contribution of the Long bar, have been neglected. Nevertheless, we believe it is useful to consider such cases because a large number of such models have been applied to our Galaxy for varied purposes. Indeed the five models we are considering here have been built by other authors for different purposes.

In the second case we will include the effect of the Long bar. Since our approach necessitates the use of an analytic potential, which has not been calculated so far for objects as complex as the bar described in Section 2.2, we will model the bar as the superposition of two bar models, a vertically very thick one which has the properties of the *COBE*/DIRBE bar and represents the boxy/peanut bulge, and a very thin one which represents the Long bar. Trials with *N*-body simulations show that this is a very reasonable approximation, no worst than other approximations standard used in such modelling. We still need to decide at what angle to place the bar major axis with respect to the Galactic Centre–Sun line. Since the measurements of

[2] In a side-on view the galaxy is viewed edge-on, with the line of sight perpendicular to the bar major axis.

[3] In the end-on view the galaxy is viewed edge-on with the line of sight along the bar major axis.

[4] A short movie, showing this bar from several viewing angles can be found in http://lam.oamp.fr/research/dynamique-des-galaxies/scientific-results/milky-way/bar-bulge/how-many-bars-in-mw/

the distance of the Long bar are quite accurate, it would be tempting to place it at 40°. Simulations, however, show that in many cases the end of the bar is not symmetric, but extends considerably further towards the leading side, in a form reminiscent of a short arm of ring segment (e.g. Athanassoula & Misiriotis 2002). This is also seen in a number of external galaxies. If it is the case for the MW as well, then observers would be measuring distances both from stars in the thin outer parts of the bar and from that leading segment and that would make the bar look as if it were at a somewhat larger angle than what it really is. The difference will not be big, maybe 5° or 10°. For this reason, we have considered many values of the angle between the bar major axis, but will use for most displays the value of 30°, while discussing what the effect of changing this angle is. Since these two bars are part of the same object, i.e. they rotate together, they should have the same pattern speed. To model the Long thin bar, we will use the same type of bar as for the thick *COBE*/DIRBE bar, but with different values of the free parameters chosen according to the available observations (see the appendix). We will refer to this set of models as case 2.

As already discussed in Section 2.2 and also in the previous paragraph, we believe that the angular separation between the *COBE*/DIRBE bar and the Long bar is an artefact due to the uncertainties of the measurements and the existence of the leading extension. Nevertheless, in order to follow these observations we will also consider the case where the angular separation between bars is of 20° (case 3). Clearly, since we assume that the pattern speeds of the two bars are the same, this situation is dynamically unstable due to the forces and torques between the two bars. We nevertheless discuss it briefly to follow the observations.

In Table 1, we give a brief summary of the main characteristics of each model. For each model (column 1), we give the type of bar included in the potential (column 2), the solar radius (column 3), the value of the pattern speed (column 4) and for each of the three cases, the corotation radius or the distance of the equilibrium point L_1 to the Galactic Centre, r_{L_1}, and the three values of bar strength, in sequence α, Q_b and Q_{t,L_1}. The latter are defined as follows.

(i) α (columns 6, 10 and 14) is the ratio of the radial force due to the bar's potential to that due to the axisymmetric background, evaluated at the solar radius and along the *COBE*/DIRBE bar major axis. We thus have

$$Q_\mathrm{r}(r) = \frac{\partial \Phi_\mathrm{b}/\partial r}{\partial \Phi_0/\partial r}, \tag{1}$$

and $\alpha = Q_\mathrm{r}(R_0)$, where Φ_b and Φ_0 denote the bar and the axisymmetric potential, respectively, and R_0 is the solar radius. This quantity is analogous to q_r in Athanassoula et al. (1983).

(ii) A similar quantity can be obtained if we use the tangential, rather than the radial bar force:

$$Q_\mathrm{t}(r) = \frac{(\partial \Phi(r,\theta)/\partial\theta)_\mathrm{max}}{r(\partial \Phi_0/\partial r)}, \tag{2}$$

where Φ is the total potential, Φ_0 is its axisymmetric part and the maximum in the numerator is calculated over all values of the azimuthal angle θ. The maximum of $Q_\mathrm{t}(r)$ over all radii shorter than the bar extent is called Q_b (columns 7, 11 and 15 in Table 1) and is often used to measure the bar strength (Buta, Block & Knapen 2003; Buta, Laurikainen & Salo 2004; Laurikainen, Salo & Buta 2004; Buta et al. 2005; Durbala et al. 2009; Manos & Athanassoula 2011). The radius where this maximum is achieved is defined as r_max, i.e. $Q_\mathrm{b} = Q_\mathrm{t}(r_\mathrm{max})$.

(iii) Q_{t,L_1} (columns 8, 12 and 16) is the value of the tangential force at the Lagrange radius or corotation, $Q_{\mathrm{t},L_1} = Q_\mathrm{t}(r = r_{L_1})$. This indicator was introduced in Paper III and was shown to correlate well with morphological features of the galaxy (such as the axial ratio of the rings or the pitch angle of spirals).

Note that the values of α and Q_{t,L_1} are evaluated at the outer parts of the bar or the disc, whereas Q_b gives the tangential force at a radius that lies inside the bar.

In the left-hand panels of Fig. 3, we show $Q_\mathrm{r}(r)$ (top panel) and $Q_\mathrm{t}(r)$ (bottom panel) for the five models with only the *COBE*/DIRBE bar, i.e. case 1. In the inlet in each panel, we make a zoom of the region around the solar radius. The grey strip marks the range between the minimum (3.6 kpc for PMM04) and the maximum (4.4 kpc for MR09) corotation radius. From the curves in the left-hand panels of Fig. 3, and also from the value of Q_{t,L_1}, we note that model Fux01 has the strongest bar around corotation, followed, in sequence by MR09, PMM04, Dehnen00 and finally GF10. Around the solar radius, both α and Q_t agree in the sequence, which from strongest to weakest is Fux01, MR09, Dehnen00, PMM04 and GF10. For models MR09, PMM04 and GF10, the region of corotation is displaced slightly outwards by the introduction of the Long bar, but it is not affected by any change in the angular separation between the two bars, as expected. Indeed this displacement is due to the mass of the Long bar and is independent of its orientation. In models Fux01 and Dehnen00 the bar is only modelled as a non-axisymmetric forcing, thus introducing no extra mass and no displacement of corotation outwards. Comparing the curves of the middle and right-hand panels of Fig. 3, at the corotation and solar regions, we note that the sequence of the models as a function of bar strength does not change. Note, however, how the introduction of the Long bar increases both Q_r and Q_t, in all models and especially in PMM04, GF10 and MR09, which have a bar that comes from a density distribution.

Table 1. Characteristics of the five analytical models. In the first and second columns, we write the name of the model and the type of bar, respectively. In the third column, give the value of the solar radius and in the fourth column, we give the value of the pattern speed. Then for each case, namely case 1 (potential with only the *COBE*/DIRBE bar), case 2 (potential with the *COBE*/DIRBE and Long bar aligned) and case 3 (potential with the *COBE*/DIRBE and Long bar at 20° of angular separation), we give the corotation radius (r_{L_1}), the radial force at the solar position (α), the maximum of the tangential force (Q_b) and the tangential force at the corotation radius (Q_{t,L_1}). The units are kpc for distance and km s^{-1} kpc^{-1} for the pattern speed.

				Case 1				Case 2				Case 3			
Model	Bar	R_0	Ω_b	r_{L_1}	α	Q_b	Q_{t,L_1}	r_{L_1}	α	Q_b	Q_{t,L_1}	r_{L_1}	α	Q_b	Q_{t,L_1}
Fux01	Quadrupole	8.	51.	4.3	0.022	0.38	0.08	4.7	0.03	0.45	0.1	4.7	0.03	0.43	0.1
MR09	Ferrers	7.1	54.	4.4	0.02	0.49	0.08	4.7	0.02	0.83	0.09	4.7	0.02	0.50	0.09
PMM04	Composite	8.5	60.	3.6	0.005	0.53	0.08	3.9	0.01	0.61	0.12	3.9	0.008	0.54	0.13
Dehnen00	Quadrupole	8.	51.	4.3	0.01	0.17	0.04	4.5	0.016	0.23	0.06	4.5	0.015	0.21	0.05
GF10	Ferrers	8.	56.	4.2	0.003	0.22	0.02	4.5	0.006	0.63	0.03	4.4	0.004	0.36	0.02

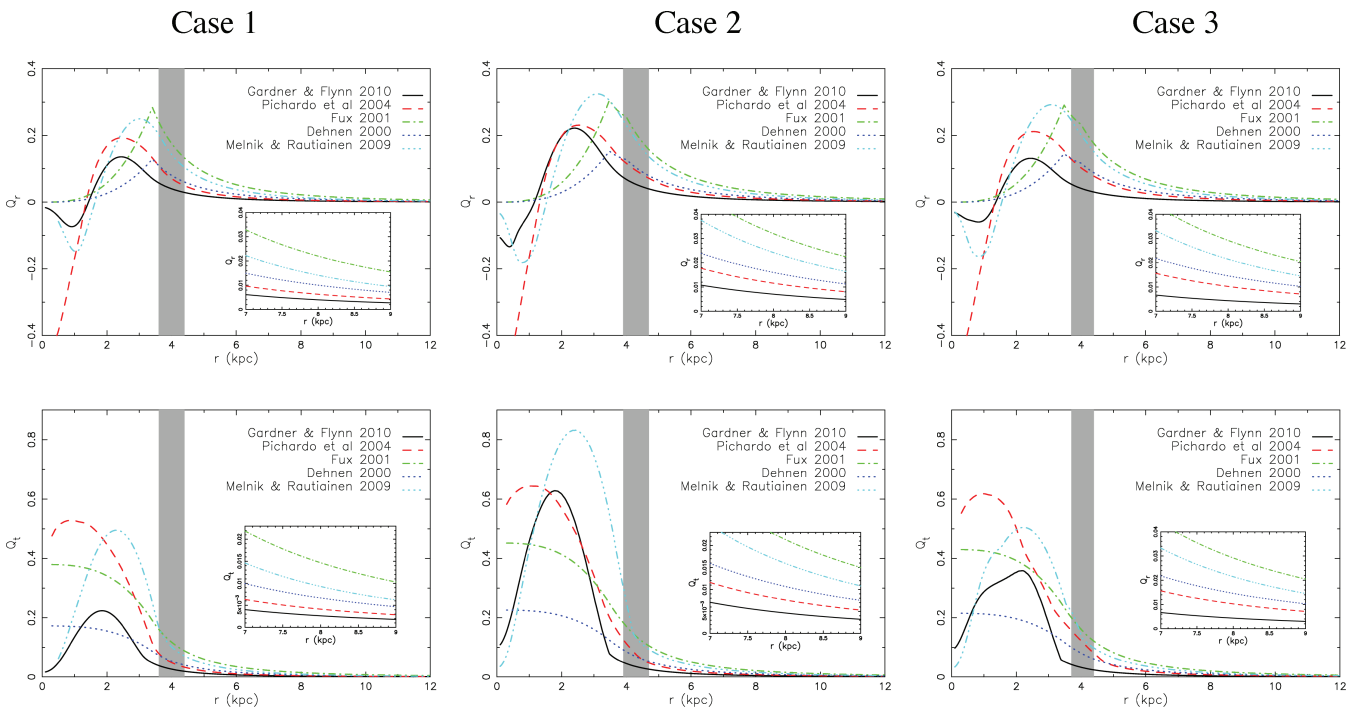

Figure 3. Radial profile of Q_r (upper panels) and Q_t (bottom panels) for the models used here. Left-hand column: case 1 with only the *COBE*/DIRBE bar; middle column: case 2 with the *COBE*/DIRBE and Long bars aligned; right-hand column: case 3 with the *COBE*/DIRBE and Long bars at an angular separation of 20°. The inlays show the solar neighbourhood region in better resolution. In all panels, the grey strip marks the corotation region (see text).

Note that the value of Q_b only reflects the behaviour of the tangential force in the inner parts of the bar. If we were interested in this region, we would use the value of Q_b as the measure of bar strength, and the sequence would be as follows: PMM04, followed by MR09, Fux01, GF10 and Dehnen00. In case 3, the introduction of the Long bar does not change the sequence, although when the two bars are aligned, case 2, the sequence, from the highest to the lowest bar strength, is MR09, GF10, PMM04, Fux01 and Dehnen00.

Since we are not interested in the innermost parts of the Galaxy, but rather in a region around corotation, we will use Q_{t,L_1} as the measure of bar strength.

3 THE INVARIANT MANIFOLDS

The models presented in the previous section are composed of an axisymmetric component and a non-axisymmetric component, the latter described by either a single bar (case 1) or two bars (cases 2 and 3), rotating clockwise with a constant angular velocity, Ω_b. In cases 2 and 3, both bars are assumed to have the same pattern speed. We will work in the reference frame where the bar is at rest and we use the convention that in this frame, the *COBE*/DIRBE bar is along the x-axis. We concentrate on the motion on the $z = 0$ plane (the Galactic equatorial plane). A full 3D study, albeit for a simple logarithmic potential, was treated in Romero-Gómez et al. (2009) and revealed that the motion in the vertical direction can be essentially described by an uncoupled harmonic oscillator, whose amplitude is relatively small and that the 3D structures do not affect the motion in the $z = 0$ plane.

Our theory is largely based on the dynamics of the Lagrangian points L_1 and L_2 of a 2D galaxy system. These are located where the first derivatives of the effective potential vanish, along the bar semimajor axis, and are unstable saddle points (Binney & Tremaine 2008). Each of them is surrounded by a family of periodic orbits, called Lyapunov orbits (Lyapunov 1949). Since these orbits are unstable they cannot trap around them quasi-periodic orbits of the same energy, so that any orbit in their immediate vicinity (in phase space) will have to escape the neighbourhood of the corresponding Lagrangian point. Not all departure directions are, however, possible. The direction in which the orbit escapes is set by what we call the invariant manifolds. These can be thought of as tubes that guide the motion of particles of the same energy as the manifolds (Koon et al. 2000; Gómez et al. 2004). In Fig. 4, we show that from each Lyapunov orbit (light grey thin curve roughly in the middle

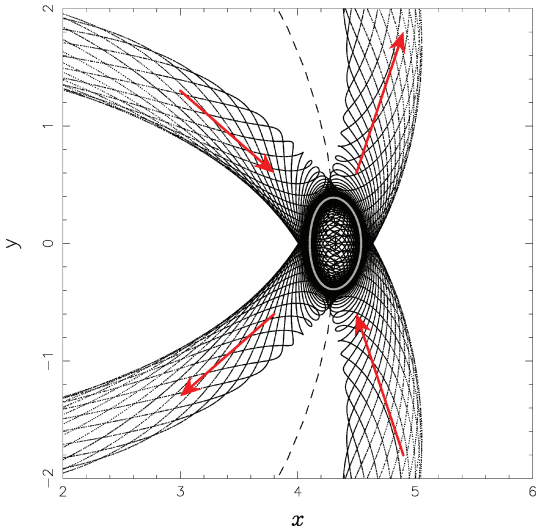

Figure 4. Dynamics around L_1. The four branches of the invariant manifolds (black curves) associated to the Lyapunov orbit (grey curve). The red arrows show the sense of circulation, while the black dashed line marks the position of the corotation radius.

of the panel), emanate four branches: two of them inside corotation (inner branches) and two of them outside it (outer branches). Along two of these branches (one inner and one outer) the mean motion is towards the region of the Lagrangian point (stable manifolds), while along the other two it is away from it (unstable manifolds). In this theory the stars travel along the orbits trapped by the manifolds.

We need to stress that the terms 'stable' and 'unstable' do not mean that the orbits that follow them are stable and unstable, respectively. In fact all the orbits that follow the manifold are chaotic, but they are in a loose way 'confined' by the manifolds, so that they stay together, at least for a few pattern rotations, in what could be called a bundle. The terms stable and unstable refer to the sense of the motion and are related to the saddle behaviour of the equilibrium points. We propose that these manifolds and orbits are the building blocks of the spirals and rings (Papers II and III). These manifolds do not exist for all values of the energy, but only for energies for which the corresponding Lyapunov periodic orbit is unstable. This means energies within a range starting from the energy of the L_1 or L_2 (E_{J,L_1}) and extending over a region whose extent depends on the potential (Skokos et al. 2002a).

The morphological and kinematical characteristics of the manifolds in external barred galaxies are studied in Papers III–V. Note that in these papers, the non-axisymmetric component consists of a single bar. The main results relevant to this study can be summarized as follows.

(i) The large-scale structure of the galaxy is related to the strength and the pattern speed of the bar (Paper III). We find that weak non-axisymmetric perturbations produce manifolds of rR_1 ring shape (an inner ring elongated around the bar and an outer ring whose principal axis is perpendicular to that of the bar), while strong non-axisymmetric perturbations produce spiral arms or other types of rings.

(ii) The range for the shape and size of both the inner and outer ring given by the models agree with that from observations, where the axial ratio of the inner ring spreads uniformly within the range 0.6–0.95, while the axial ratio of the outer ring falls within the range of 0.7–1 (Buta 1986). Furthermore, we find a strong anticorrelation between the axial ratio of the rings and the bar strength.

(iii) The default number of spiral arms given by the manifolds is two, since they are associated with the number of saddle points of the model. The typical orientation is trailing, i.e. following the unstable branch of the manifolds, and their shape reproduces the characteristic arm winding often observed in external galaxies, i.e. the spiral arms first unwinds and then returns to the bar region.

(iv) The formation of the manifolds, and therefore of the rings and spirals, depends on the existence of the saddle Lagrangian points. These appear when we perturb the axisymmetric potential with a non-axisymmetric component. We have applied this theory to barred galaxies, but the saddle Lagrangian points can be due to other non-axisymmetric perturbations, such as spiral perturbations.

(v) In potentials with a strong $m = 4$ component of the forcing, manifolds can also account for four-armed spirals.

(vi) We also studied the behaviour of collisional manifolds using a simple model in which the particles within a manifold lose energy (Papers III and V). We compared collisional and collisionless manifolds and found that they have very similar shapes, at least for rings and for the first half turn of spirals. The collisional rings, however, are thinner, i.e. more concentrated, than their collisionless counterparts.

(vii) Bars are known to evolve secularly, becoming longer and stronger while slowing down. As a result, the Lagrangian points move outwards and the Q_{t,L_1} increase. This has important implications for manifolds, whose shape and location will change adiabatically with time. Furthermore, it will bring material to the Lagrangian points, replenishing the mass reservoirs that fill the manifolds. In the case of rings, once material is trapped in the manifolds, it can stay there indefinitely, if the model is stationary, while any increase in the bar strength can trap more material into the manifolds.

4 THE INNER PART OF THE DISC

Here we study the morphology and kinematics of the models mentioned in Section 2. To compare them morphologically, in Section 4.1 we show the invariant manifolds, 'tubes' that guide the motion of the stars, of a given energy level. To study the kinematics, in Section 4.2, we use the orbits trapped by the manifolds, since these are the ones that really trace the kinematics. In this case, and in order to make the plots clear and clean, we will consider the orbits of minimum energy, since for higher energies, the orbits overlap and the area they outline grows thicker (Paper I). Finally, in Section 4.3, we discuss how the manifolds reproduce the observables of the inner part of the Galaxy, i.e. the region between 2 and 6 kpc, using the up-to-date MW potentials.

4.1 The morphology

Fig. 5 illustrates how the invariant manifolds change as a function of the pattern speed and the bar mass/amplitude for two of the bar types considered here, namely the composite bar (top panel) and the ad hoc quadrupole bar (bottom panel). The results for the Ferrers bar are similar to the composite bar and can be seen by comparing with fig. 4 of Paper III. Note that only the *COBE*/DIRBE bar is modelled here (case 1) and that as we increase the pattern speed of a model, the Lagrangian radius moves inwards, and the manifolds become attached to the bar. To better understand the plots, we give the ratio of the Lagrangian radius over the bar scalelength. For the composite bar models, the bar scalelength is fixed to $a = 3.13$ kpc (see the appendix) and the Lagrangian radius is varied, therefore, the ratio r_L/a increases from left to right from 1.47 to 2. On the other hand, for the quadrupole bar models, the ratio r_L/a is fixed to 1.25, so the bar length-scale is different in each panel. In the latter case, the ratio is inside the range determined by hydrodynamic simulations $r_L/a = 1.2 \pm 0.2$ (Athanassoula 1992), while in the former, it is outside it. We cannot, however, extend our search to smaller r_L/a values because this would entail too big pattern speed values (Gerhard 2011).

In Fig. 6 we plot the invariant manifolds for all case 1 models that we consider here, i.e. up-to-date MW models with only the *COBE*/DIRBE bar and we use the set of parameters that the authors consider to describe best the MW disc potential. In each panel we plot the invariant manifolds of a given energy. The morphology does not depend on the energy value chosen, provided this is near the Lagrangian point energy (Paper I).[5] The panels are ordered from left to right, from the strongest bar model to the weakest bar model, namely Fux01, MR09, PMM04, Dehnen00 and GF10, according to the Q_{t,L_1} measure of the force (see Table 1). All cases present both an inner and an outer ring and can be classified as

[5] The energy chosen for each model is $|(E_{J,\mathrm{Fux01}} - E_{J,L_1})/E_{J,L_1}| = 6.6 \times 10^{-4}$, $|(E_{J,\mathrm{MR09}} - E_{J,L_1})/E_{J,L_1}| = 2.5 \times 10^{-3}$, $|(E_{J,\mathrm{PMM04}} - E_{J,L_1})/E_{J,L_1}| = 6.5 \times 10^{-4}$, $|(E_{J,\mathrm{Dehnen00}} - E_{J,L_1})/E_{J,L_1}| = 7.2 \times 10^{-3}$ and $|(E_{J,\mathrm{GF10}} - E_{J,L_1})/E_{J,L_1}| = 7.2 \times 10^{-3}$.

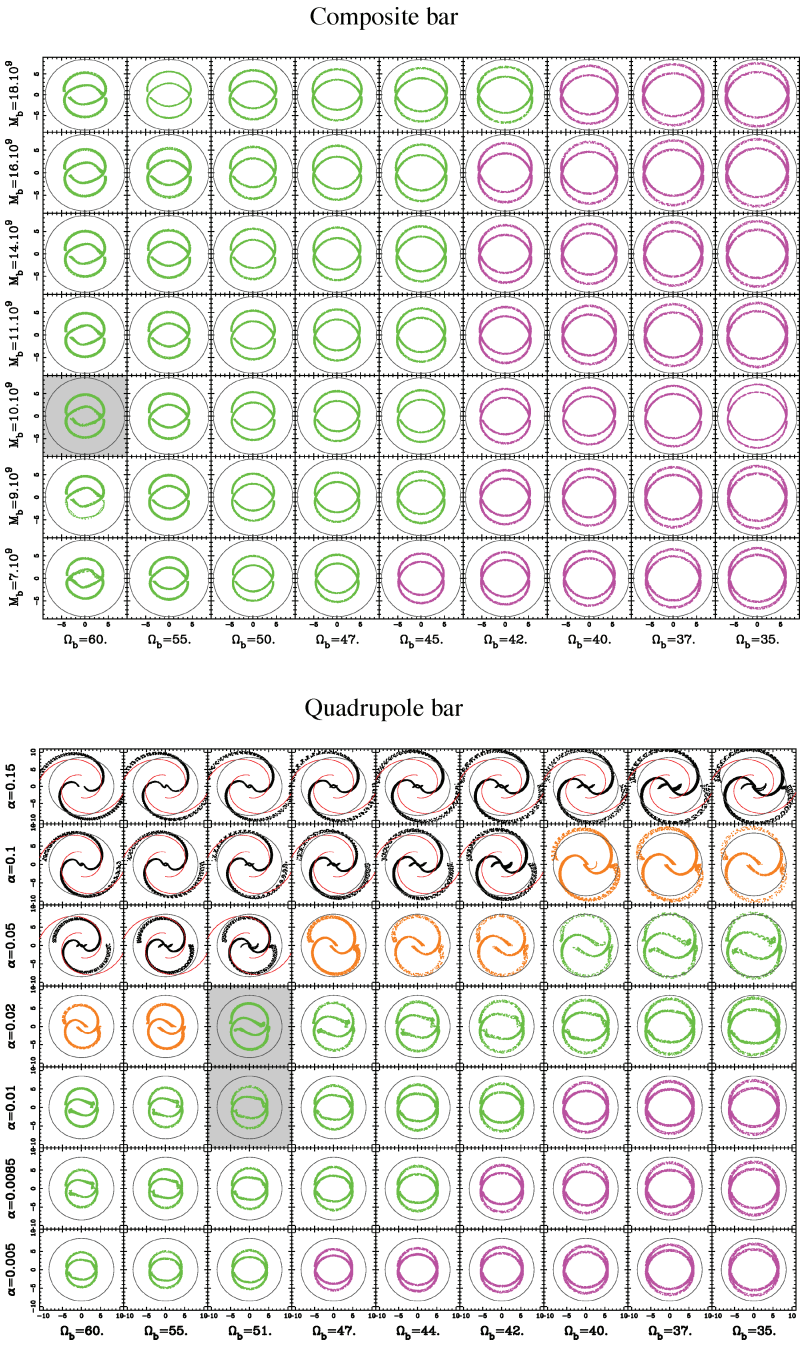

Figure 5. 2D parameter study of the composite and quadrupole bar models for case 1. On the x-axis we decrease the pattern speed from left to right. On the y-axis we increase the bar strength from bottom to top, from a bar mass $M_\mathrm{b} = 7 \times 10^9$ to 18×10^9 $\mathrm{M}_\odot$ for the composite bar or from $\alpha = 0.005$ to 0.15 for the quadrupole bar. The thin black circle in each panel marks the solar radius. Top panel: the composite bar model. The panel with grey background corresponds to model PMM04. Bottom panel: the quadrupole bar model. The panels with grey background correspond to model Fux01 (top: $\alpha = 0.02$ and $\Omega_\mathrm{b} = 51$) and Dehnen00 (bottom: $\alpha = 0.01$ and $\Omega_\mathrm{b} = 51$).

rR_1 ring morphologies. The axial ratio of the rings, however, is clearly different from one model to another. In columns 2–5 of Table 2 we give the axial ratio and the major diameter of the inner and outer rings. Dehnen00 and GF10 have an inner ring axial ratio that falls well within the observational range (0.6–0.95) for the SB galaxies (Buta 1986). In contrast, the inner rings in Fux01, MR09 and PMM04 are too elongated with axial ratios ranging from $d_\mathrm{i}/D_\mathrm{i} =$ 0.43–0.5, respectively. In the particular cases of MR09 and PMM04, whose bar potential is built from a density distribution, the locus of the inner manifolds falls well inside the bar ellipsoid, so that, when self-gravity would be considered, the two could merge, as discussed in Paper IV. Therefore, we cannot consider the inner rings of MR09 and PMM04 as proper inner rings surrounding the bar and this justifies their low axial ratio. The bar in Fux01 is ad hoc and we cannot confirm this fact. For Dehnen00 and GF10, the axial ratio of the inner ring increases with decreasing bar strength, from being oval, $d_\mathrm{i}/D_\mathrm{i} = 0.66$ for Dehnen00, to more circular, $d_\mathrm{i}/D_\mathrm{i} = 0.77$ for GF10, in good agreement with what was found in Paper IV. There

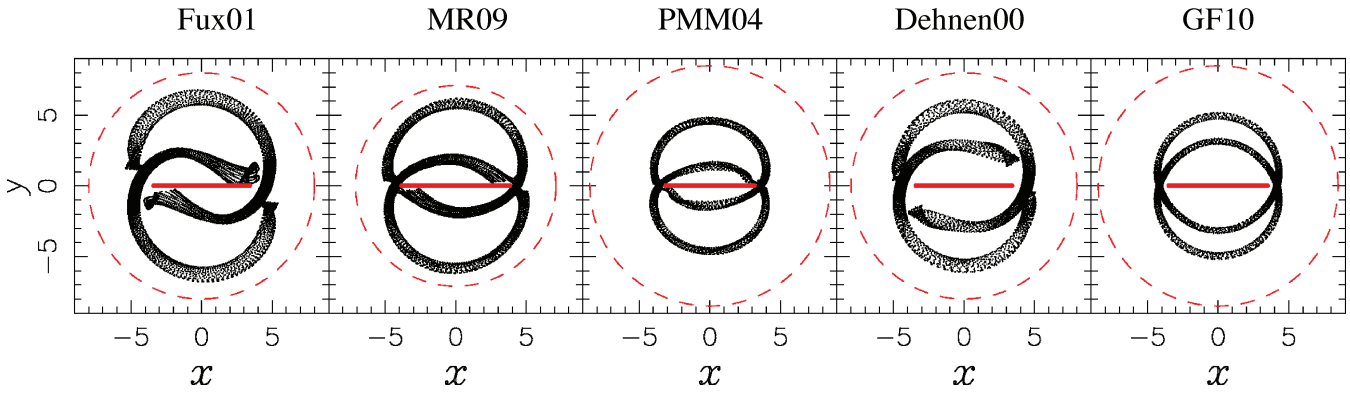

Figure 6. Invariant manifolds for the five selected bar potentials and case 1. From left to right: Fux01, MR09, Dehnen00, PMM04 and GF10. The thick solid red line marks the position and length of the bar. In the case of the ad hoc potentials, it marks the bar scalelength. The thin dashed red circle marks the solar radius adopted by the respective authors.

Table 2. Sizes of the inner and outer rings in the three cases considered, from left to right, only the *COBE*/DIRBE bar (case 1), *COBE*/DIRBE and Long bar aligned (case 2) and *COBE*/DIRBE and Long bar at $\phi = 20^\circ$ (case 3). For each of the cases and for each of the models, we give, in the first and second columns, the axial ratio and the major diameter of the inner ring, d_i/D_i and D_i, respectively, (in kpc), while in the third and fourth columns, we give the same values for the outer ring, d_o/D_o and D_o, respectively.

	Case 1				Case 2				Case 3			
Model	d_i/D_i	D_i	d_o/D_o	D_o	d_i/D_i	D_i	d_o/D_o	D_o	d_i/D_i	D_i	d_o/D_o	D_o
Fux01	0.43	4.6	0.74	6.9	0.31	4.7	0.68	7.2	0.31	4.6	0.74	7.1
MR09	0.46	4.3	0.75	6.2	0.40	4.7	0.71	6.8	0.32	4.6	0.78	6.9
PMM04	0.50	3.6	0.78	5.0	0.32	3.9	0.76	6.6	0.41	3.7	0.78	5.5
Dehnen00	0.66	4.5	0.80	6.1	0.54	4.5	0.76	6.3	0.50	4.5	0.82	6.3
GF10	0.77	4.2	0.86	5.3	0.72	4.4	0.81	5.7	0.78	4.1	0.82	5.1

are also differences in the size. The inner ring in Fux01, MR09 and PMM04 is very elongated, as mentioned above, not reaching 3 kpc along the minor axis. On the other hand, Dehnen00 and GF10 have a major diameter of $D_i = 4.5$ and 4.2 kpc, respectively.

The axial ratio of the outer ring in the five models falls well within the observational range (0.7–1) for SB galaxies (Buta 1986) and correlates with the bar strength as measured by Q_{t,L_1}, as found for other models in Paper IV. Fux01, with the strongest bar, has the more eccentric outer ring, $d_o/D_o = 0.74$, while GF10, with the weakest bar, has a more circular ring with $d_o/D_o = 0.86$. The major diameter is around $D_o = 6$ kpc. In Fux01 the outer ring reaches 6.9 kpc along the major diameter, and in MR09 and Dehnen00 it is around 6 kpc, while GF10 and PMM04 have the smallest outer rings with a major diameter of 5.3 and 5.0 kpc, respectively.

In case 2, where the Long bar is aligned to the *COBE*/DIRBE bar, the global morphology is still that of an rR_1 ring, but there is an effect on the shape and kinematics of the rings (see Section 4.2). The axial ratio of the outer ring decreases approximately by 5 per cent in the mean, compared to that of case 1, while the axial ratio of the inner ring decreases on average by 20 per cent (see columns 6–9 of Table 2). Changing the angle between the bar major axis and the direction of the Galactic Centre–Sun line makes no difference to this result. In case 3, the axial ratio of the outer ring, d_o/D_o, essentially does not change compared to that of case 2. The inner ring, on the contrary, gets more elongated with a mean decrease of the axial ratio, d_i/D_i, of about 30 per cent compared to the values given by case 1, in agreement with the elongated 3-kpc arm obtained by Habing et al. (2006) from the distribution of maser stars in the inner MW. As discussed in Paper IV this can be due to the fact that we include orbits that form the outer parts of the bar. The size of the global structure is similar to that of the single bar model (see columns 10–13 of Table 2). This means that there is in general an agreement with what is observed in external galaxies.

4.2 The kinematics

This section is devoted to the analysis of the kinematics provided by the manifolds in the selected models. Fig. 7 shows the line-of-sight heliocentric velocity given at each galactic longitude, hereafter (l, v) diagram, obtained from CO observations (Dame et al. 2001). The main features found in the inner 2–6 kpc of the Galaxy are marked with solid and dashed lines, namely the near and far 3-kpc arms and the overdensity crossing the (l, v) at $l = 0^\circ$ and $v = 0\,\mathrm{km\,s^{-1}}$ (GMR). The rest of the features are related to the central part of the Galaxy or to the outer arms, so we will not consider them in our comparisons. Note also that these features were observed in the CO, while we compare them to collisionless manifolds. This, nevertheless, is possible since in Papers III and V we showed that the shape of collisional and collisionless manifolds does not differ much, at least for rings and for the first half turn of spirals (except for the width, which is smaller in the collisional cases). Furthermore, in external galaxies where it is easy to check, we note that the shapes of the gaseous and stellar rings are very similar, with the notable difference that the rings in the young stars are thinner than the ones in the old stars, in good agreement with our calculations. Finally, in external galaxies there are few, if any, purely gaseous rings with no stellar component. This would anyway be contrived, since it would involve a strong concentration of gas which would not form stars. We can thus proceed with our comparisons.

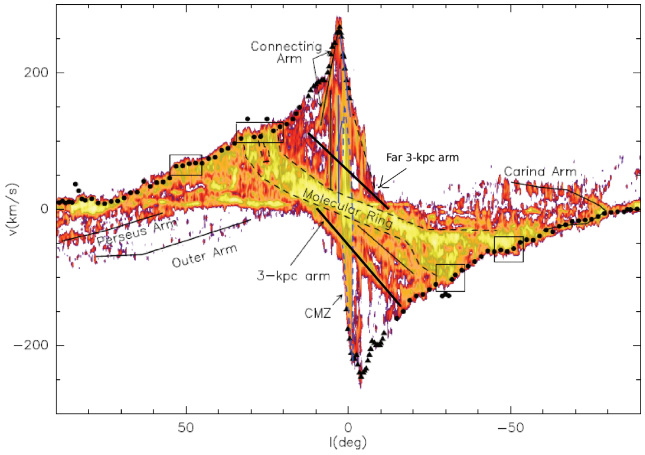

Figure 7. The (l, v) diagram obtained from the observations of Dame et al. (2001) and Dame & Thaddeus (2008), as plotted by Rodríguez-Fernández & Combes (2008). The line-of-sight velocity is given with respect to the local standard of rest (LSR). The solid lines trace the position of some remarkable features such as the locus of the spiral arms, the 3-kpc arm and the connecting arm. The black dashed lines indicate the contour of the GMR. The solid circles are the terminal velocities measurements of Fich, Blitz & Stark (1989) using CO, while the triangles are the terminal velocities determined from the H I data of Burton & Liszt (1993). The boxes mark the position of the Sagittarius, Scutum, Norma and Centaurus tangent points, located, respectively, at $l \sim 50^\circ$, $\sim 30^\circ$, $\sim -30^\circ$ and $\sim -50^\circ$.

For each model, we compute the orbits trapped by the manifolds with the energy closest to the energy of L_1 (minimum energy for the manifolds to exist), and we show them in the first column of Figs 8–10, for the *COBE*/DIRBE bar only (case 1), the two-bar models aligned (case 2) and the two-bar models with and angular separation of 20° (case 3), respectively. In the middle and right-hand panels of the same figures, we plot the (l,v) diagram separately for the inner and outer branches of the rings, respectively. The colours mark the different parts of the ring. We also show in a thin dotted black line the axisymmetric component of the terminal velocity curve, i.e. the maximum line-of-sight velocity at a given longitude. The black solid and dashed lines are extracted from Fig. 7 and trace the position of the near and far 3-kpc arm and of the GMR, respectively.

The kinematic features in the (l, v) diagram that should be characterized and taken into account for the subsequent comparison with observations (Section 4.3) are as follows: first, where and by how much the non-axisymmetric component exceeds the circular terminal velocities; secondly, the shape of the lines traced on the diagram compared to the overdensities on the observed one; thirdly, the non-zero value of the line-of-sight velocity at $l = 0^\circ$ for these overdensities (expansion or contraction in the radial Sun–centre direction).

In several models, we observe that the velocities of the orbits in the manifolds exceed the circular terminal velocities at low longitudes. For example, the inner rings of Fux01 and MR09 in all three cases (one or two bars) exceed the terminal velocities at low longitudes (see the second column of Figs 8–10). This is due to the non-axisymmetric motions, but can in some cases be excessive (see discussion in Section 4.3). It is also worth mentioning that the introduction of the Long bar changes the (l,v) diagram in almost all cases. In case 2, where the Long bar is aligned with the *COBE*/DIRBE bar, in all models except for GF10, the velocities of the inner ring exceed the circular terminal velocity curve, due to the excess of mass introduced. In Fux01 and MR09, however, the maximum velocity is well above the terminal curve. In case 3, it increases the velocities in models PMM04, Dehnen00 and GF10 to values slightly exceeding the terminal velocities at certain longitudes.

Table 3 summarizes the line-of-sight velocities along the Galactic Centre–Sun line, i.e. $l = 0^\circ$. We see that the range of variation for this velocity is 6–50 km s^{-1} in absolute value, for the models in case 1. The introduction of the Long bar in case 2 increases the line-of-sight velocity at $l = 0^\circ$ in all models and, in case 3, in all models but PMM04, where it slightly decreases.

The kinematics along the outer ring also provides information about the deviation from the circular velocity curve. Fig. 11 shows the relative deviation of the tangential velocity in the inertial frame from the circular velocity for the orbits in all models with the *COBE*/DIRBE bar. The angle θ is defined as the azimuthal galactocentric angle with origin on the Galactic Centre–Sun line and measured clockwise. The circular velocity at a given radius is given by the axisymmetric component in the case of Fux01 and Dehnen00 models and by the axisymmetric component plus the $m = 0$ component of the bar in MR09, GF10 and PMM04 models. Note that in each case, the deviation from a flat rotation curve is less than 20 km s^{-1}, in agreement with fig. 6 of Kranz, Slyz & Rix (2001).

4.3 Towards a manifold model of the inner MW

In the previous sections we analysed in an exhaustive way the results given by the manifolds for a wide set of models including the possibility of modelling only the *COBE*/DIRBE bar or both the *COBE*/DIRBE bar and the Long bar. We claim that in general the manifolds can interpret the observables both morphologically and kinematically. We now compare the results with the MW observations and analyse in detail what manifold models are more likely to reproduce the 3-kpc arm and the GMR.

The observed characteristics of the 3-kpc arm are twofold: it is elongated along the bar and it has non-zero velocities at $l = 0^\circ$ (-53 km s^{-1} for the near arm and 56 km s^{-1} for the far arm; Dame & Thaddeus 2008), although other studies based on ammonia and water in absorption give a value of -43 km s^{-1} (Wirström et al. 2010). This sets a tentative estimate of the error bar of about 10 km s^{-1}. Among the set of models considered here, we can say that when only the *COBE*/DIRBE bar is considered (case 1) MR09 and PMM04 reproduce this feature (see Table 3, where Fux01, Dehnen00 and GF10 have absolute values below 15 km s^{-1}).

The introduction of the Long bar, either aligned or misaligned, in the models makes the inner ring more elongated and increases the velocities along $l = 0^\circ$, suggesting that the models with the two bars have a tendency to better reproduce the observed line-of-sight velocity of the 3-kpc arm (see Table 3). There is a big uncertainty in the model parameters, including the angular position of the bar in case 2. Increasing the angle from 20° to 40° makes the line-of-sight velocities in the region of the 3-kpc arm to increase in absolute value, i.e. increases the rectangular shape of the orbits in the (l,v) diagram, while it decreases the size of the necklace-shaped feature corresponding to the GMR. In the three selected cases, we can see that several models can reach the observed line-of-sight velocities, and even exceed them, whereas Dehnen00 and GF10 clearly do not fit the observations.

From Figs 8–10 we observe that Fux01 in all three cases and MR09 in cases 2 and 3 have velocities that highly exceed the terminal velocity curve and, therefore, they do not satisfy one of the main constraints of the (l,v) diagram. This fact can be due to two reasons. First, these models have strong bars, i.e. the bar perturbation is quite

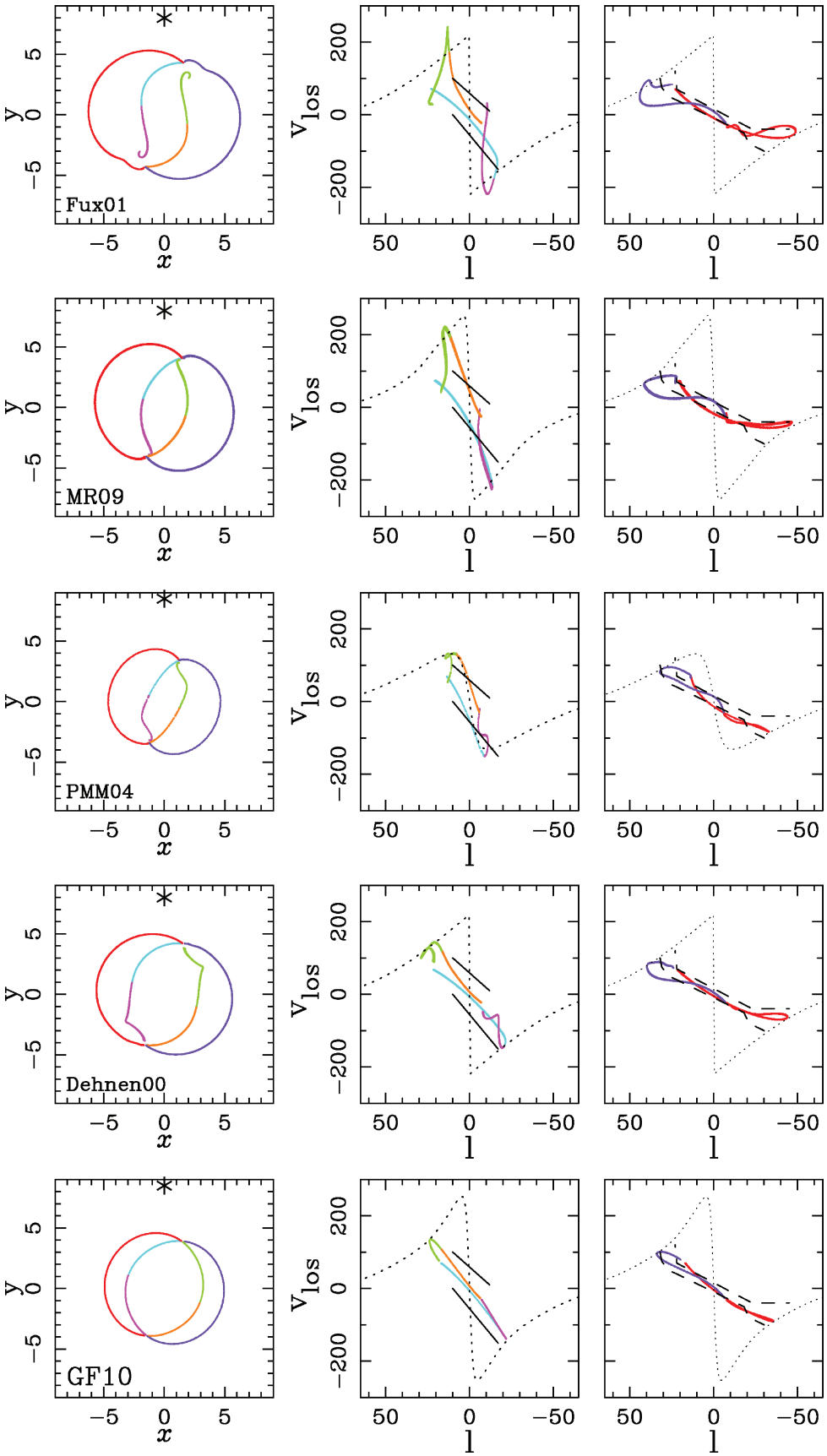

Figure 8. The (l, v) diagrams of the five selected models with only the *COBE*/DIRBE bar, i.e. case 1: from top to bottom, Fux01, MR09, PMM04, Dehnen00 and GF10 model. Left-hand column: orbits in the (x, y) plane, the colours showing different parts of the rings; middle and right-hand column: (l, v) diagram of the inner and outer manifolds, respectively. The circular terminal velocity is given by the black dotted line.

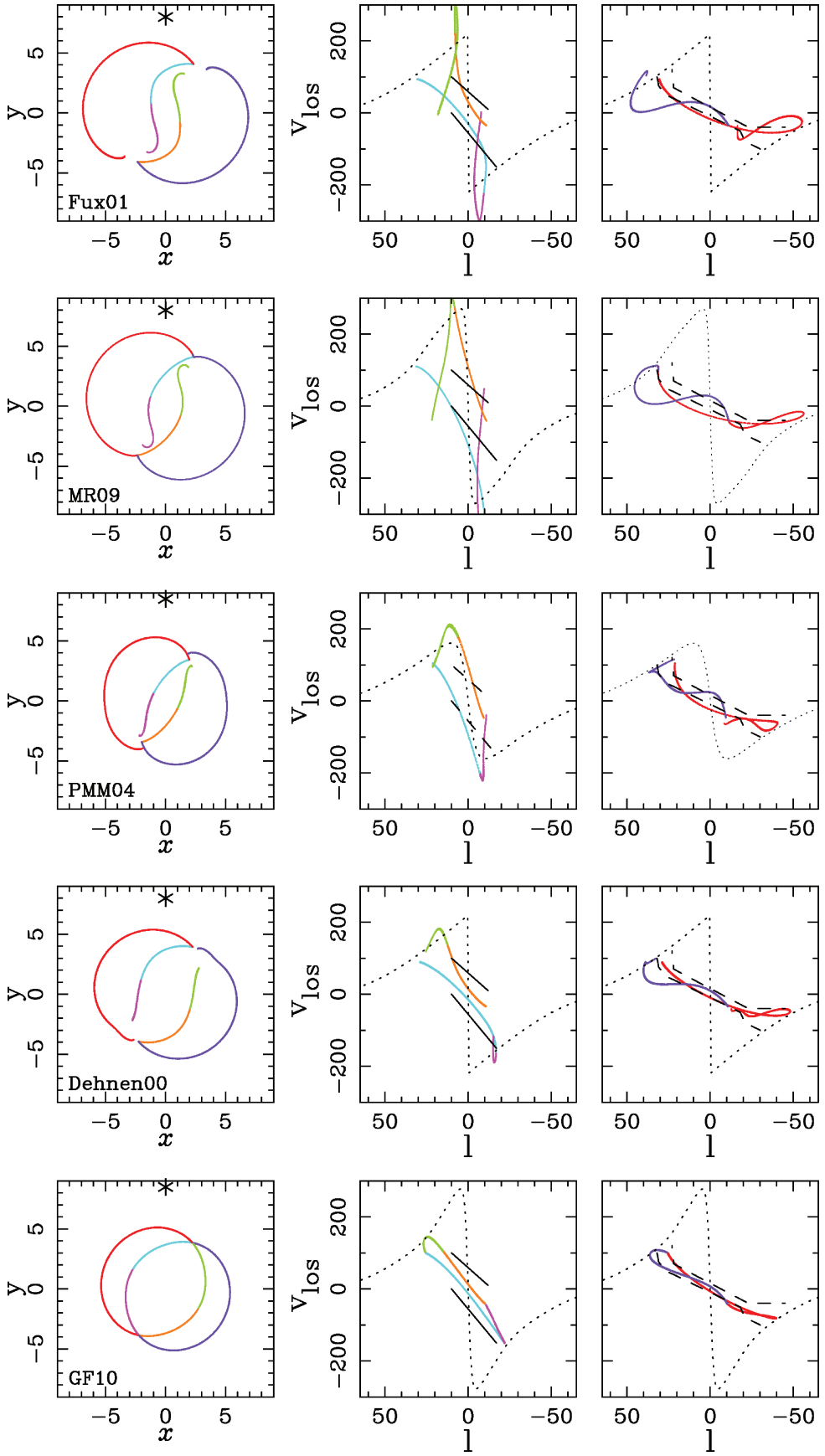

Figure 9. As in Fig. 8, but now for case 2, where the two bars are aligned at 30° from the Galactic Centre–Sun line.

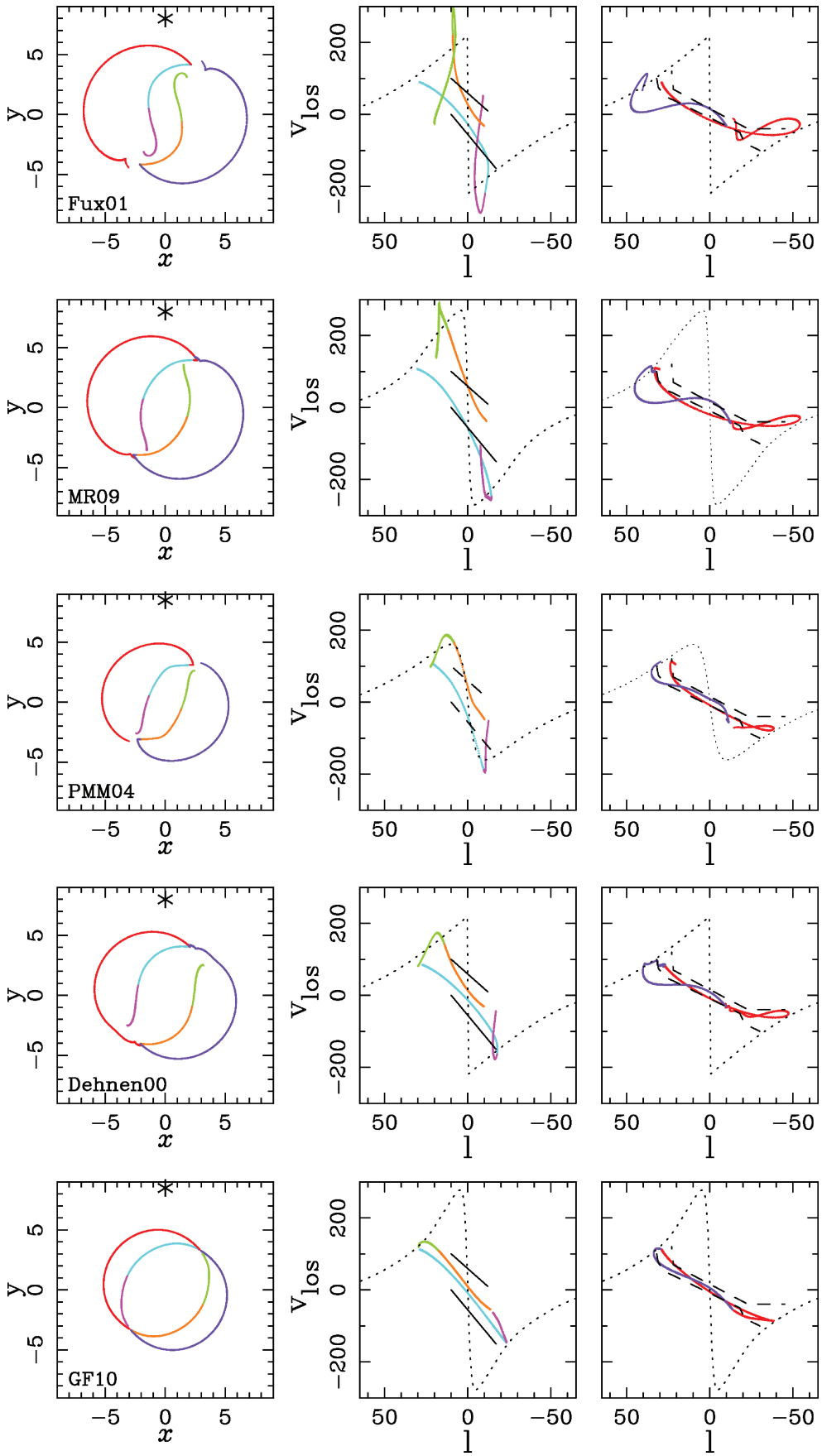

Figure 10. As in Fig. 8, but now for case 3, i.e. for models with two bars with an angular separation of 20°.

Table 3. Line-of-sight velocities with respect to the LSR at $l = 0°$. N stands for the near 3-kpc arm, while F stands for the far 3-kpc arm. Units are in km s^{-1}.

Model	Case 1		Case 2		Case 3	
	v_{los} N	v_{los} F	v_{los} N	v_{los} F	v_{los} N	v_{los} F
Fux01	−15.	13.	−30.	30.	−27.	28.
MR09	−46.	44.	−108.	109.	−59.	58.
PMM04	−51.	50.	−94.	95.	−42.	42.
Dehnen00	−7.	6.	−15.	15.	−15.	13.
GF10	−6.	6.	−13.	12.	−9.	9.

noticeable in the outer parts. The second reason is morphological and related to the previous one. The orbits trapped in the inner ring resemble the cuspy x_1 orbits of the bar, responsible for the maximum in the terminal velocity curves (Binney et al. 1991). So the inner branches of the orbits are in the immediate vicinity of the orbits of the bar, making an increase of the velocity at low longitudes.

All the above discussion suggests that at least some of the model parameters may not be appropriate for the MW, and most of them may not be optimum. Indeed, they were selected in the papers described in the appendix so as to give optimum results for the *COBE*/DIRBE bar only, and not for the two bars together. We have nevertheless followed them here because they are the standard reference models in the field. In a future paper we will search for the parameter values which are optimum for the *COBE*/DIRBE and Long bar system.

The spatial locus of the GMR is not well established. Clemens et al. (1988) claim that the peak emission of the GMR is at ∼5.5 kpc, while Binney & Merrifield (1998), Dame et al. (2001) and Rathborne et al. (2009) suggest that it is located around (1/2)R_0. Clemens et al. (1988) believe that the GMR is an almost circular ring with a pitch angle of about 4°, while other authors (Fux 1999; Dame et al. 2001; Rodríguez-Fernández & Combes 2008) favour the possibility that the molecular ring is composed of several inner spiral arm segments rooted in the central bar. Kinematically, though, it is somewhat better constrained. It defines an overdensity in the (l,v) diagram, crossing the plane from ∼100 km s^{-1} and $l \sim 30°$ to ∼ −100 km s^{-1} and $l \sim -40°$, passing through the origin and having a typical necklace shape. Morphologically, the outer branches of the manifolds in most of the cases have a size appropriate to the GMR, although Fux01, MR09 and Dehnen00 have a major diameter closer to the Sun's position than to halfway from the Galactic Centre. The shape varies from one model to another, the models of Dehnen00, PMM04 and GF10 (with only one bar or with two bars) having the shape nearest to circular. Kinematically, not all models fit the enhancements related to the GMR. The manifold branches plotted in red in Figs 9 and 10 (cases 2 and 3) fit well inside the dashed lines in all models, while the dark blue branches lie inside the dashed lines only for models GF10 and PMM04. Fux01, MR09 and Dehnen00 the blue line makes a loop that resembles the overdensity found between $l = 30°$ and 40° [see fig. 5 of Rathborne et al. 2009, where they plot the (l,v) diagram given by the ^{13}CO emission of the molecular clouds and clumps of the Boston Galactic Ring Survey]. Note, in addition, that the angular separation between the bars does not affect the global shape of the outer manifolds, either morphologically or in the (l,v) diagram.

5 OBTAINING THE OUTER SPIRAL ARMS

As mentioned in the Introduction, one of the main features of the MW is the presence of two stellar massive spiral arms (Benjamin et al. 2005). In this section, we discuss the *COBE*/DIRBE bar models focusing on the parameters necessary in order for the manifolds to reproduce a two-armed spiral shape.

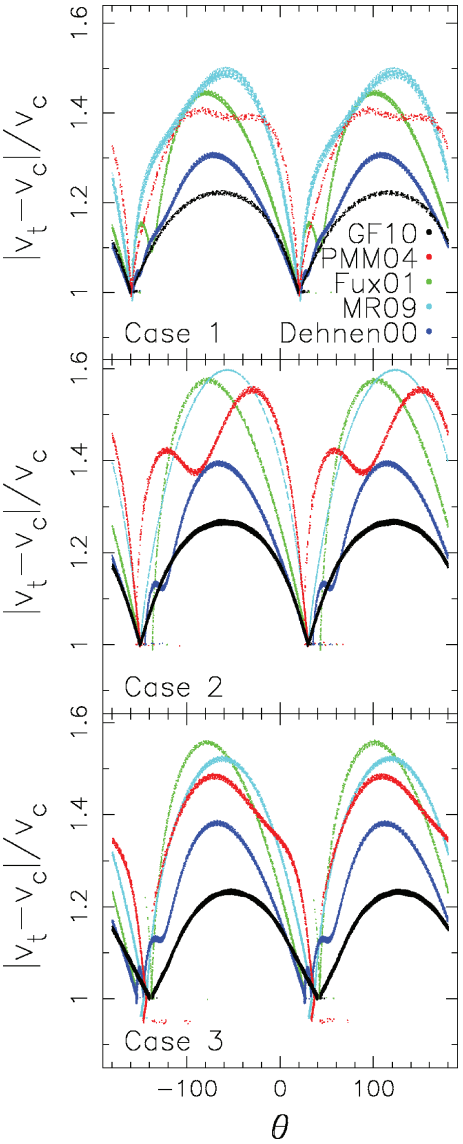

Figure 11. Relative deviation of the tangential velocities in the inertial frame with respect to the circular velocity of the outer ring as a function of the azimuthal galactocentric angle θ. Top panel: case 1, models with only the *COBE*/DIRBE bar. Middle panel: case 2, two-bar models aligned. Bottom panel: case 3, two-bar models at an angular separation of 20°. The colours represent the same type of models in all panels.

In Section 3 and Paper II we showed that in a barred galaxy potential, the two parameters that influence most the shape of the invariant manifolds in the outer parts are the bar mass (or amplitude of the $m = 2$ component for quadrupole bars) and its pattern speed. In subsequent papers, we analysed the effect of the variation of both parameters and showed that the resultant gross global morphology is not model dependent, and that, for all models, faster and more massive bars produce more open spiral arms, while slower and less massive bars produce symmetric outer rings (see Fig. 5 and Paper III).

In the previous section, we computed the invariant manifolds for five selected MW models with the default parameters chosen by the

authors. In all cases, the global morphology is that of an rR_1 ring whose extension does not reach the solar radius. As seen in Fig. 5, if we want to reproduce the outer spiral arms of the Galaxy using orbits confined by the manifolds, we should significantly increase the bar mass or strength, and the pattern speed of each model. In fig. 8 of Paper III, we plot the different models considered as a function of the strength parameter Q_{t,L_1}. We observed that the different morphologies are grouped as a function of Q_{t,L_1}, so if the bar model has $Q_{\mathrm{t},L_1} < 0.1$ we have R_1 outer rings, while for $0.1 < Q_{\mathrm{t},L_1} < 0.2$ the model gives R_1' pseudo-rings, and for $Q_{\mathrm{t},L_1} > 0.2$ it gives spirals and the other type of rings (R_2 and R_1R_2). So we need to use model parameters that give a value of Q_{t,L_1} of around 0.2, or larger. Note that this value is significantly larger than the values given in Table 1. We will see if this is a plausible option for the MW.

In the case of quadrupole bars, the minimum values of α and Ω_b necessary to obtain tightly wound spiral arms are 0.05 and $50\,\mathrm{km\,s^{-1}\,kpc^{-1}}$, respectively (bottom panel of Fig. 5). A model with two open spiral arms that crosses the solar radius can be obtained with $\alpha \geq 0.1$ and $\Omega_\mathrm{b} \geq 40\,\mathrm{km\,s^{-1}\,kpc^{-1}}$. Even though the pattern speed falls within the range found by simulations (Englmaier & Gerhard 1999), the bar strength is too high. Remember that α is the radial force along the bar semimajor axis and at the solar radius. It means that with a quadrupole model and a flat rotation curve, we need a bar whose strength is about 10 per cent of that of the disc at the solar radius. Besides, the Q_b parameter of this model is 2.08 far outside the observed range (Block et al. 2004). If we vary the shape of the rotation curve and we make it slightly decreasing in the outer parts ($\beta = -0.2$), we can obtain two open spiral arms with $\alpha \geq 0.075$ and $\Omega_\mathrm{b} \geq 57\,\mathrm{km\,s^{-1}\,kpc^{-1}}$. The radial force of the bar in the solar neighbourhood is still quite high but it gives $Q_\mathrm{b} = 0.63$, implying a strong bar, but within the observed range (Block et al. 2004). This might indicate that if we want to reproduce the spiral arms using manifolds, it seems necessary to have a decreasing rotation curve in the outer parts. A recent study conducted by Xue et al. (2008) analysed more than 2400 stars from the Sloan Digital Sky Survey (SDSS) and concluded that it is indeed possible that the rotation curve of the MW decreases in the outer parts, by a factor within the range $\beta = (-0.2, -0.1)$, compatible with the suggested model. Other studies (Brand & Blitz 1993) suggest that the rotation curve of the MW could be slightly increasing in the outer parts, meaning that we should need stronger bars in order to obtain open spiral arms with manifolds.

In the case of composite bars, the force decreases very abruptly in the outer parts of the disc, see Fig. 3. In order to obtain values of Q_{t,L_1} of the order of 0.1 or 0.2 we have to increase the pattern speed up to at least $\Omega_\mathrm{b} \sim 75\,\mathrm{km\,s^{-1}\,kpc^{-1}}$ for a bar mass of $1.4 \times 10^{10}\,\mathrm{M_\odot}$. If, on the other hand, we decrease the bar axial ratio, also related to the bar mass, to $b/a = 0.25$, we can obtain values of Q_{t,L_1} of the order of 0.1 with a bar mass of $\sim 2.0 \times 10^{10}\,\mathrm{M_\odot}$ and a pattern speed of $\Omega_\mathrm{b} \sim 70\,\mathrm{km\,s^{-1}\,kpc^{-1}}$. Nevertheless, the value of Q_{t,L_1} is still too low. The case of Ferrers bars is analogue to the composite bar.

The main conclusion here is that it seems that in any case the *COBE*/DIRBE bar is not strong enough to make two open spiral arms that could reach the outer parts of the disc. Even though the introduction of the Long bar makes the inner branches of the manifolds more elongated (Section 4.1), it does not change the previous conclusions. Models with an extra component to the potential, for example a spiral forcing, should be explored in the future as a possible option to induce spiral arms through manifolds.

6 SUMMARY AND CONCLUSIONS

In this paper, we applied the invariant manifolds theory for the first time to the MW. We first presented a thorough discussion about whether the Long bar and the *COBE*/DIRBE bar are, respectively, the primary and the secondary bar of a double bar system in our Galaxy. We dismissed this alternative, because their properties are in strong disagreement with the properties of double bars in external galaxies and with those in simulations. We then considered the alternative that the *COBE*/DIRBE bar and the Long bar are simply *parts of the same bar*, the former being the boxy/peanut bulge and the latter the thin outer parts of the bar. We compared the morphology thus obtained with that of external barred galaxies, with that obtained from orbital structure and with simulations, and found very good agreement in all cases. We also proposed some reasonable possibilities to explain the fact that observations indicate a misalignment between the major axes of the *COBE*/DIRBE bar and of the Long bar.

We then selected five characteristic models in the literature that include the *COBE*/DIRBE bar, and, to account for recent observations and the above-mentioned possibility, we have also considered the case with an additional Long bar. We analyse the models, first in terms of forces, and then we compute the manifolds in three cases, namely when only the *COBE*/DIRBE bar is modelled (case 1), when the two bars are aligned at 30° from the Galactic Centre–Sun line, as observed in a large amount of external galaxies (case 2), and when the two bars have an angular separation of 20° according to the observations (case 3). Note, however, that in the models discussed here, both bars rotate at the same pattern speed, which makes case 3 dynamically unstable.

Regarding the questions formulated in the Introduction, we confirm that the observed features of the inner parts of the Galaxy, more specifically the 3-kpc arms and the GMR, can be plausibly interpreted using manifolds. The morphological and kinematic analysis shows that the inner and outer rings described by the manifolds can well represent the 3-kpc arms and the GMR of the inner parts of the Galaxy, respectively. Not all models, however, are suitable to describe both features at the same time and in both ways. In general, the GMR is well reproduced by all models in all three cases, but the 3-kpc arms depend more on the characteristics of the potential.

We can tentatively conclude that the two bars of the Galaxy, i.e. the *COBE*/DIRBE and the Long bar, are necessary to reproduce the observables and, in this case, among the five models, the ones with less strong bars, namely PMM04, Dehnen00 and GF10 have a better fit. Another conclusion of this work is that the value of the angular separation between the bars does introduce changes both in the morphology of the rings and in the (l, v) diagram.

We also analysed in detail what bar parameters would be necessary so that the manifolds have a spiral arms morphology concluding that, for quadrupole bars, a stronger bar is necessary, while for the composite and the Ferrers bars, the force decreases too abruptly in the outer parts of the disc, and it is difficult to obtain open spiral arms by only increasing the bar mass or its pattern speed. In the case, though, where the global morphology would be one with two spiral arms, the rR_1 configuration would be lost. This suggests that the most probable solution in the manifold framework would be a more complex potential with one or two bars in the inner part and a spiral further out.

In a future paper we will revisit the most successful of the models considered here and vary their main parameters – i.e. the mass and

the pattern speed of the bar, and the angle of the bar major axis with the Galactic Centre–Sun line – searching for the values that give the best fits to the observations.

ACKNOWLEDGMENTS

We thank Albert Bosma for interesting discussions and encouragement, Jean-Charles Lambert for his help with glnemo viewings and Peter Erwin for sharing with us his double bar data. We also thank J. Beckman, P. Garzón, P. L. Hammersley, M. López-Corredoira and T. J. Mahoney for very interesting discussions on the Long bar and on the basic ideas of Section 2.2, following a seminar given by EA in IAC in 2006. This work was supported by the MICINN (Spanish Ministry of Science and Innovation) – FEDER through grant AYA2009-14648-C02-01 and CONSOLIDER CSD2007-00050. TA acknowledges funding support from the European Research Council under ERC-StG grant GALACTICA-24027.

NOTE ADDED IN PRESS

After this paper was submitted, we became aware from a talk of another work analogous to what we present in Section 2.2. This is now published in Martinez-Valpuesta & Gerhard (2011), and its conclusions are in good agreement with ours.

REFERENCES

Alard C., 2001, A&A, 379, L44
Allen C., Santillán A., 1991, Rev. Mex. Astron. Astrofis., 22, 255
Antoja T., Valenzuela O., Pichardo B., Moreno E., Figuera F., Fernández D., 2009, ApJ, 700, L78
Athanassoula E., 1992, MNRAS, 259, 345
Athanassoula E., 2005, MNRAS, 358, 1477
Athanassoula E., 2006, preprint (astro-ph/0610113)
Athanassoula E., 2008, in Wada K., Combes F., eds, Mapping the Galaxy and Nearby Galaxies. Springer-Verlag, Berlin, p. 47
Athanassoula E., Beaton R. L., 2006, MNRAS, 370, 1499
Athanassoula E., Misiriotis A., 2002, MNRAS, 330, 35
Athanassoula E., Bienaymé O., Martinet L., Pfenniger D., 1983, A&A, 127, 349
Athanassoula E., Romero-Gómez M., Masdemont J. J., 2009a, MNRAS, 394, 67 (Paper III)
Athanassoula E., Romero-Gómez M., Bosma A., Masdemont J. J., 2009b, MNRAS, 400, 1706 (Paper IV)
Athanassoula E., Romero-Gómez M., Bosma A., Masdemont J. J., 2010, MNRAS, 407, 1433 (Paper V)
Baba J., Saitoh T. R., Wada K., 2010, PASJ, 62, 1413
Babusiaux C., Gilmore G., 2005, MNRAS, 358, 1309
Benjamin R. A. et al., 2005, ApJ, 630, L149
Bettoni D., Galletta G., 1994, A&A, 281, 1
Binney J., 1981, MNRAS, 196, 455
Binney J., Merrifield M., 1998, Galactic Astronomy. Princeton Univ. Press, Princeton, NJ
Binney J., Tremaine S., 2008, Galactic Dynamics, 2nd edn. Princeton Univ. Press, Princeton, NJ
Binney J., Gerhard O. E., Stark A. A., Bally J., Uchida K. I., 1991, MNRAS, 252, 210
Binney J., Gerhard O. E., Spergel D., 1997, MNRAS, 288, 365
Bissantz N., Gerhard O., 2002, MNRAS, 330, 591
Bissantz N., Englmaier P., Gerhard O., 2003, MNRAS, 340, 949
Block D. L., Buta R., Knapen J. H., Elmegreen D. M., Elmegreen B. G., Puerari I., 2004, AJ, 128, 183
Brand J., Blitz L., 1993, A&A, 275, 67
Burton W. B., Liszt H. S., 1993, A&A, 274, 765
Buta R., 1986, ApJS, 61, 609
Buta R., Block D. L., Knapen J. H., 2003, AJ, 126, 1148
Buta R., Laurikainen E., Salo H., 2004, AJ, 127, 279
Buta R., Vasylyev S., Salo H., Laurikainen E., 2005, AJ, 130, 506
Cabrera-Lavers A., Hammersley P. L., González-Fernández C., López-Corredoira M., Garzón F., Mahoney T. J., 2007, A&A, 465, 825
Cabrera-Lavers A., González-Fernández C., Garzón F., Hammersley P. L., López-Corredoira M., 2008, A&A, 491, 781
Chakrabarty D., 2007, A&A, 467, 145
Churchwell E. et al., 2009, PASP, 121, 213
Clemens D. P., Sanders D. B., Scoville N. Z., 1988, ApJ, 327, 139
Combes F., Debbasch F., Friedli D., Pfenniger D., 1990, A&A, 233, 82
Contopoulos G., Papayannopoulos T., 1980, A&A, 92, 33
Dame T. M., Thaddeus P., 2008, ApJ, 683, L143
Dame T. M., Thaddeus P., 2011, ApJ, 734, L24
Dame T. M., Hartmann D., Thaddeus P., 2001, ApJ, 547, 792
Debattista V. P., Gerhard O., Sevenster M. N., 2002, MNRAS, 334, 355
Dehnen W., 2000a, AJ, 119, 800 (Dehnen00)
Dehnen W., 2000b, ApJ, 536, L39
Dehnen W., 2002, J. Comput. Phys., 179, 27
Durbala A., Buta R., Sulentic J. W., Verdes-Montenegro L., 2009, MNRAS, 397, 1756
Dwek E. et al., 1995, ApJ, 445, 716
Englmaier P., Gerhard O., 1999, MNRAS, 304, 512
Erwin P., 2011, Mem. Soc. Astron. Ital., Suppl., 18, 145
Erwin P., Sparke L., 2002, AJ, 124, 65
Ferrers N. M., 1877, Q. J. Pure Applied Math., 14, 1
Fich M., Blitz L., Stark A. A., 1989, ApJ, 342, 272
Freudenreich H. T., 1998, ApJ, 492, 495
Fux R., 1999, A&A, 345, 787
Fux R., 2001, A&A, 373, 511 (Fux01)
Gardner E., Flynn C., 2010, MNRAS, 405, 545 (GF10)
Gerhard O., 2002, in Da Costa G. S., Jerjen H., eds, ASP Conf. Ser. Vol. 273, The Dynamics, Structure and History of Galaxies: A Workshop in Honour of Professor Ken Freeman. Astron. Soc. Pac., San Francisco, p. 73
Gerhard O., 2011, Mem. Soc. Astron. Ital. Suppl., 18, 185
Gómez G., Koon W. S., Lo M. W., Marsden J. E., Masdemont J. J., Ross S. D., 2004, Nonlinearity, 17, 1571
Green J. A. et al., 2011, ApJ, 733, 27
Habing H. J., Sevenster M. N., Messineo M., van de Ven G., Kuijken K., 2006, A&A, 458, 151
Hammersley P. L., Garzón F., Mahoney T. J., López-Corredoira M., Torres M. A. P., 2000, MNRAS, 317, L45
Heller C. H., Shlosman I., Athanassoula E., 2007, ApJ, 657, L65
Hernquist L., 1990, ApJ, 356, 359
Hernquist L., 1993, ApJS, 86, 389
Kent S. M., 1992, ApJ, 387, 181
Kerr F. J., 1964, AJ, 69, 547
Koon W. S., Lo M. W., Marsden J. E., Ross S. D., 2000, Chaos, 10, 427
Kranz T., Slyz A., Rix H.-W., 2001, ApJ, 562, 164
Laine S., Shlosman I., Knapen J. H., Peletier R. F., 2002, ApJ, 2002, 567, 97
Laurikainen E., Salo H., Buta R., 2004, ApJ, 607, 103
López-Corredoira M., Cabrera-Lavers A., Gerhard O., 2005, A&A, 439, 107
López-Corredoira M., Cabrera-Lavers A., Mahoney T. J., Hammersley P. L., Garzón F., González-Fernández C., 2007, AJ, 133, 154
Lütticke R., Dettmar R.-J., Pohlen M., 2000, A&A, 362, 435
Lyapunov A., 1949, Ann. Math. Studies, 17
Manos T., Athanassoula E., 2011, MNRAS, 415, 629
Martinez-Valpuesta I., Gerhard O., 2011, ApJ, 734, L20
Martinez-Valpuesta I., Shlosman I., Heller C., 2006, ApJ, 637, 214
Matsumoto T., Hayakawa S., Koizumi H., Murakami H., Uyama K., Yamagami T., Thomas J. A., 1982, in Riegler G. R., Blandford R. D., eds,

Proceedings of the Workshop, The Galactic Center. Am. Inst. Phys., New York, p. 48
Melnik A. M., Rautiainen P., 2009, Astron. Lett., 35, 609 (MR09)
Minchev I., Boily C., Siebert A., Bienaymé O., 2010, MNRAS, 407, 2122
Miyamoto M., Nagai R., 1975, PASJ, 27, 533
Patsis P., Skokos Ch., Athanassoula E., 2002, MNRAS, 337, 578
Patsis P. A., Kalapotharakos C., Grosbol P., 2010, MNRAS, 408, 22
Pfenniger D., 1984, A&A, 134, 373
Pichardo B., Martos M., Moreno E., 2004, ApJ, 609, 144 (PMM04)
Quillen A. C., Kuchinski L. E., Frogel J. A., Depoy D. L., 1997, ApJ, 481, 179
Rathborne J. M., Johnson A. M., Jackson J. M., Shah R. Y., Simon R., 2009, ApJS, 182, 131
Rodríguez-Fernández N. J., Combes F., 2008, A&A, 489, 115
Romero-Gómez M., Masdemont J. J., Athanassoula E., García-Gómez C., 2006, A&A, 453, 39 (Paper I)
Romero-Gómez M., Athanassoula E., Masdemont J. J., García-Gómez C., 2007, A&A, 472, 63 (Paper II)
Romero-Gómez M., Masdemont J. J., García-Gómez C., Athanassoula E., 2009, Communications Nonlinear Sci. Numer. Simulations, 14, 4123
Sevenster M. N., 2002, AJ, 123, 2788
Shen J., Debattista V. P., 2009, ApJ, 690, 758
Skokos Ch., Patsis P. A., Athanassoula E., 2002a, MNRAS, 333, 847
Skokos Ch., Patsis P. A., Athanassoula E., 2002b, MNRAS, 333, 861
Stanek K. Z., Udalski A., Szymanski M., Kaluzny J., Kubiak M., Mateo M., Krzeminski W., 1997, ApJ, 477, 163
Tsoutsis P., Kalapotharakos C., Efthymiopoulos C., Contopoulos G., 2009, A&A, 495, 743
Vallée J. P., 2008, AJ, 135, 1301
Weiland J. L. et al., 1994, ApJ, 425, L81
Weiner B. J., Sellwood J. A., 1999, ApJ, 524, 112
Wirström E. S. et al., 2010, A&A, 522, A19
Xue X. X. et al., 2008, ApJ, 684, 1143
Zhao H., 1996, MNRAS, 278, 488

APPENDIX A:

Here we describe the models we used throughout the paper, namely models with a quadrupole bar (Dehnen00; Fux01), a composite bar (PMM04) and a Ferrers bar (Ferrers 1877; MR09; GF10). We also give a brief description of the simulation used in Section 2.2.

A1 The quadrupole bar model: Fux01 and Dehnen00

The quadrupole model consists of the superposition of an axisymmetric component given by a simple power-law rotation curve and an $m = 2$ type potential for the bar, as in Dehnen00 and Fux01. We refer to these models in the text as Dehnen00 and Fux01, respectively.

The potential corresponding to a power-law rotation curve is

$$\Phi_0(R) = v_0^2 \begin{cases} (2\beta)^{-1}(R/R_0)^{2\beta}, & \beta \neq 0, \\ \ln(R/R_0), & \beta = 0, \end{cases} \tag{A1}$$

where $R_0 = 8\,\mathrm{kpc}$ denotes the Galactocentric distance to the Sun and v_0 the local circular speed. Since in this paper we compare the two Galaxy models, we will keep the original values of R_0 and v_0, namely 8 kpc and $220\,\mathrm{km\,s^{-1}}$ for Dehnen00, and 8 kpc and $200\,\mathrm{km\,s^{-1}}$ for Fux01. The parameter β is related to the shape of the rotation curve, with $\beta = 0$ for a flat rotation curve, $\beta < 0$ for a falling rotation curve and $\beta > 0$ for a rising rotation curve. We use flat rotation curves in this paper, unless otherwise stated. In the case of falling rotation curves, we use a value of $\beta = -0.2$.

The bar is described as the $m = 2$ component of the Fourier decomposition of the potential: $\Phi_\mathrm{b}(R, \theta) = A(R)\cos(2\theta)$, where

$$A(R) = A_\mathrm{b} \begin{cases} \left(\frac{R}{R_\mathrm{b}}\right)^3 - 2, & R \leq R_\mathrm{b}, \\ -\left(\frac{R_\mathrm{b}}{R}\right)^3, & R \geq R_\mathrm{b}, \end{cases} \tag{A2}$$

where R_b and A_b are the size and the amplitude of the bar. In both models, $R_\mathrm{b} = 0.8 r_{L_1}$ and $r_{L_1} = 4.35\,\mathrm{kpc}$. This Lagrangian radius together with the rotation curve given by equation (A1), corresponds to a pattern speed of $\Omega_\mathrm{b} = 51\,\mathrm{km\,s^{-1}\,kpc^{-1}}$.

The authors measure the strength parameter of the bar by the ratio of the forces due to the bar and to the axisymmetric power-law component at the Sun Galactocentric radius on the bar's semimajor axis:

$$\alpha = 3\frac{A_\mathrm{b}}{v_0^2}\left(\frac{R_\mathrm{b}}{R_0}\right)^3. \tag{A3}$$

Note that this measure is dimensionless, it is directly related to the bar amplitude and it is related to equation (1) by $\alpha = Q_\mathrm{r}(R_0)$. When the Long bar is introduced in the potential, it is described also with an $m = 2$ component of the Fourier decomposition of the potential with $R_\mathrm{bl} = 0.92 r_{L_1}$, $r_{L_1} = 4.35\,\mathrm{kpc}$ and $\alpha_\mathrm{l} = 0.6\alpha$.

A2 The composite bar model: PMM04

The composite bar is an analytical model designed to fit the density profile of the bar given by *COBE*/DIRBE. Again, it consists of the superposition of an axisymmetric component and a bar. The axisymmetric component is the result of the superposition of a bulge, a disc and a dark matter halo. The potential we used is based on the one considered by Allen & Santillán (1991) to fit the axisymmetric component of the MW. The bulge and the disc are modelled using a Miyamoto–Nagai potential (Miyamoto & Nagai 1975):

$$\Phi_\mathrm{bl}(R, z) = -\frac{M_1}{\left(R^2 + z^2 + b_1^2\right)^{1/2}}, \tag{A4}$$

where (R, z) are the cylindrical coordinates, $M_1 = 1.4 \times 10^{10}\,\mathrm{M_\odot}$ is the bulge mass and $b_1 = 0.3873$ is the bulge scalelength:

$$\Phi_\mathrm{d}(R, z) = -\frac{M_2}{\left(R^2 + \left[a_2 + \left(z^2 + b_2^2\right)^{1/2}\right]^2\right)^{1/2}}, \tag{A5}$$

where $M_2 = 8.56 \times 10^{10}\,\mathrm{M_\odot}$ is the disc mass, $a_2 = 5.3178$ and $b_2 = 0.25$ are the radial and vertical scalelengths, respectively. The dark matter halo is described using a spherical potential:

$$\Phi_\mathrm{h}(r) = -\frac{M(r)}{r} - \frac{M_3}{1.02 a_3}\left[-\frac{1.02}{1 + (r/a_3)^{1.02}} + \ln\left(1 + (r/a_3)^{1.02}\right)\right]_\mathrm{r}^{100}, \tag{A6}$$

where the halo radius is 100 kpc, $M_3 = 10.7 \times 10^{10}\,\mathrm{M_\odot}$, which makes the total mass of the halo $M(100\,\mathrm{kpc}) = 8.002 \times 10^{11}\,\mathrm{M_\odot}$, and $a_3 = 12$ is its scalelength.

The parameters are chosen so that the total mass of the axisymmetric component is $9 \times 10^{11}\,\mathrm{M_\odot}$, the rotation curve flattens at approximately $200\,\mathrm{km\,s^{-1}}$, setting the Galactocentric distance to the Sun $R_0 = 8.5\,\mathrm{kpc}$ and the circular velocity at the Sun's position to $v_0 = 220\,\mathrm{km\,s^{-1}}$.

The bar component is taken from PMM04. The density distribution is obtained to match the observations from *COBE*/DIRBE.

The bar is the result of the superposition of prolate spheroids with density:

$$\rho_{\rm b}(R_{\rm s}) = \rho_0 \begin{cases} \sec h^2(R_{\rm s}) & R_{\rm s} \leq R_{\rm end_s}, \\ \sec h^2(R_{\rm s}) {\rm e}^{-\left((R_{\rm s}-R_{\rm end_s})^2/h^2_{\rm end_s}\right)} & R_{\rm s} \geq R_{\rm end_s}, \end{cases} \tag{A7}$$

where $R_{\rm s} = ((x^2/a_x^2) + ((y^2 + z^2)/a_y^2))^{1/2}$. The parameters a_x and a_y are the scalelengths of the bar and are fixed to 1.7 and 0.54 kpc, respectively. The constants $R_{\rm end_s}$ and $h_{\rm end_s}$ are defined as $a_{\rm bar}/a_x$ and $h_{\rm end}/a_x$, respectively. The authors fix $a_{\rm bar} = 3.13$ kpc and $h_{\rm end} = 0.46$ kpc, as the values of the length of the bar and its scaleheight. The bar is divided in three regions to better describe the density. The first two have a fall of $\sec h^2$ and the third has a Gaussian fall that starts where the bar ends. This implies a steep but smooth decrease in the density in the outer parts. The bar mass is fixed to $M_{\rm b} = 10^{10}\,{\rm M}_\odot$ and $\Omega_{\rm b} = 60\,{\rm km\,s^{-1}\,kpc^{-1}}$. The model parameters of the Long bar, when included in the potential, are $a = 4.5$ kpc, $b/a = 0.24$ and $M_{\rm bl} = 0.6M_{\rm b} = 6 \times 10^9\,{\rm M}_\odot$.

A3 The Ferrers bar model: MR09 and GF10

The third bar model we use is a Ferrers bar as used by MR09 and GF10. The potential is described by the superposition of an axisymmetric plus a bar-like component. The axisymmetric component considered by the two pairs of authors is slightly different even though both have a flat rotation curve.

In MR09, the axisymmetric part of the potential has two components: a bulge and a halo. The bulge potential is a Plummer sphere (Binney & Tremaine 2008). The bulge mass is fixed to $1.22 \times 10^{10}\,{\rm M}_\odot$ and its scalelength to 0.31 kpc. The halo is described by its rotation curve as

$$v^2(r) = v_{\rm max}^2 \frac{r^2}{r^2 + r_{\rm c}^2}, \tag{A8}$$

where $v_{\rm max} = 251.6\,{\rm km\,s^{-1}}$ is the asymptotic maximum of the halo rotation curve and $r_{\rm c} = 8$ kpc is its core radius.

In GF10, the axisymmetric part of the potential has three components: a bulge, a disc and a dark halo. The bulge is a superposition of two Plummer spheres, with masses 3×10^9 and $1.6 \times 10^{10}\,{\rm M}_\odot$, respectively, and scalelengths 2.7 and 0.42 kpc, respectively. The halo is described by an axisymmetric logarithmic potential with asymptotic velocity fixed to $220\,{\rm km\,s^{-1}}$ and core radius 8.5 kpc. Finally, the disc results of the superposition of three Miyamoto–Nagai discs (Miyamoto & Nagai 1975) with masses 7.704×10^{10}, -6.848×10^{10} and $2.675 \times 10^{10}\,{\rm M}_\odot$, respectively, and radial scalelengths 5.81, 17.43 and 34.84 kpc, respectively. The vertical scalelength is the same for the three discs and it is fixed to 0.3 kpc.

As mentioned above, in both models, the bar component is described by a Ferrers ellipsoid (Ferrers 1877), whose density distribution is described by the expression

$$\rho = \begin{cases} \rho_0(1 - m^2)^n, & m \leq 1, \\ 0, & m > 1, \end{cases} \tag{A9}$$

where $m^2 = x^2/a^2 + y^2/b^2$. The parameter n measures the degree of concentration of the bar and ρ_0 measures its central concentration. It is related to the bar mass via the expression

$$M_{\rm b} = 2^{2n+3}\pi a b^2 \rho_0 \Gamma(n+1)\Gamma(n+2)/\,\Gamma(2n+4). \tag{A10}$$

In MR09, the authors fix $n = 1$, $a = 3.82$ kpc, $b = 1.2$ kpc and $M_{\rm b} = 1.82 \times 10^{10}\,{\rm M}_\odot$. The default value for the pattern speed is $\Omega_{\rm b} = 53\,{\rm km\,s^{-1}\,kpc^{-1}}$. In GF10, the authors fix $n = 2$, $a = 3.5$ kpc, $b = 1.4$ kpc and $M_{\rm b} = 10^{10}\,{\rm M}_\odot$, and the default value for the pattern speed is $\Omega_{\rm b} = 55.9\,{\rm km\,s^{-1}\,kpc^{-1}}$. The model parameters for the Long bar, when included in the potential, are $a = 4.5$ kpc, $b/a = 0.15$ kpc and $M_{\rm b} = 1.1 \times 10^{10}\,{\rm M}_\odot$ for MR09 and $a = 3.9$ kpc, $b/a = 0.15$ kpc and $M_{\rm bl} \sim 0.6M_{\rm b} = 6 \times 10^9\,{\rm M}_\odot$ for GF10.

A4 The simulation in Section 2.2

The simulation discussed in Section 2.2 is part of the library of N-body simulations run by EA, but was not made specifically to model the MW, and is only intended for illustration purposes. In the initial conditions the disc has an exponential horizontal profile and a $\sec h^2$ vertical one. The halo is described by equation (2.2) of Hernquist (1993) and the bulge by a Hernquist sphere (Hernquist 1990). It was run using the public version of the gyrfalcon code (Dehnen 2000b, 2002). The resolution for Fig. 1 was enhanced using the technique described by Athanassoula (2005) and made use of the glnemo2 display software, written by J.-C. Lambert. The same software was also used to create the short movies.

This paper has been typeset from a TEX/LATEX file prepared by the author.